On the mechanisms of modifying the structure of turbulent homogeneous shear flows by dispersed particles

A. M. Ahmed and S. Elghobashi[a)]
Mechanical and Aerospace Engineering Department, University of California, Irvine, California 92697

(Received 16 February 2000; accepted 20 July 2000)

The present study is concerned with answering the question: What are the physical mechanisms responsible for the modification of the turbulence structure by solid particles dispersed in a homogeneous shear flow? We employ DNS (direct numerical simulations) to examine the effects of the two-way interaction between the two phases on the turbulence structure. Our results indicate that particles affect the rate of production of turbulence energy via modifying the vorticity dynamics. It is known that regions of large production rate of turbulence energy are sandwiched between counter rotating vortices whose vorticity, ω_s, is aligned with the axes of the longitudinal vortex tubes. These longitudinal vortex tubes are strongly inclined toward the streamwise direction due to the imposed mean shear. The stronger ω_s is, the larger the production rate. The dispersed solid particles modify the alignment of the local vorticity vector, $\boldsymbol{\omega}$, with the axis of the longitudinal vortex tube. Increasing this alignment increases ω_s, which in turn augments the turbulence production rate, and vice versa. In addition, due to the enhanced strain rate of the carrier fluid by the particles, the dissipation rate of turbulence energy is always increased. The particles also reduce the alignment of the vorticity vector with the intermediate eigenvector (β) of the strain rate tensor. This reduction in alignment is due to an increase in the rotational term and particle-source term in the governing equation of the cosine of the angle between the vorticity vector and the intermediate strain eigenvector. © *2000 American Institute of Physics.* [S1070-6631(00)50411-5]

I. INTRODUCTION

Particle-laden turbulent shear flows occur in a wide variety of practical applications and thus have received considerable attention during the past few decades, resulting in a number of numerical and experimental studies. However, due to the complexity of these practical flows, there are no mathematical models at present that can accurately predict their properties. The complexity stems from the fact that turbulence itself (without dispersed particles) is not completely understood, and particles considerably increase that complexity. With the advent of powerful supercomputers, direct numerical simulations (DNS) have become a viable tool for studying particle-laden turbulent flows in simple configurations. However, due to the necessity of resolving all the relevant turbulence length- and time scales, DNS is still limited to moderate Reynolds number flows.

Experimental and DNS studies of particle-laden turbulent flows show that particles modify the turbulence structure and the temporal development of its kinetic energy. Rogers and Eaton[1] studied experimentally the turbulence modulation due to particles in a planar turbulent boundary layer. They found that particles of Reynolds number ≈ 5 and mass loading of 20% cause a significant reduction of the turbulence kinetic energy. This reduction was observed in all resolved turbulence scales. Rashidi *et al.*[2] conducted a flow visualization of a turbulent channel flows laden with particles. They found that polystyrene particles of 1100 μm diam *increase* the turbulence intensity by increasing the number of wall ejections. Smaller polystyrene particles of 120 μm diam *decreased* the turbulence intensity by decreasing the number of wall ejections.

The number of DNS studies concerned with turbulence modulation (two-way coupling) by dispersed particles is quite small. A review of these studies can be found in the paper by McLaughlin.[3] Squires and Eaton[4] used DNS to study the two-way interaction between particles and stationary (forced) homogeneous isotropic turbulence in zero gravity. They found that particles increase the turbulence dissipation and reduce the turbulence kinetic energy. They, also, found that the tendency of particles to accumulate in low vorticity or high strain regions decreases for light particles and increases for heavy particles. Elghobashi and Truesdell[5] studied the effect of particles on the spectrum of turbulence energy in isotropic turbulence, using DNS with 96^3 mesh points. They found that for particles in gravity, a reverse energy cascade takes place where the energy is transferred from the large wave numbers to small wave numbers. Recently, Maxey *et al.*[6] used DNS to study particles–turbulence interaction and presented a new method to calculate the two-way coupling source term, in which the particles force is distributed within a narrow envelope centered around the particle's position. Pan and Banerjee[7] used a pseudospectral method to study the modulation of turbulence in a channel flow laden by solid particles. They found that particles smaller than the Kolmogorov scale in the near wall region suppress the turbulence while larger particles enhanced it. They attributed these modifications to the reduc-

[a)]Electronic mail: selghoba@uci.edu

tion of the sweep frequency by small particles and the increase of the sweep frequency by large particles. A sweep event occurs when the fluid velocity fluctuation is positive in the streamwise direction and negative in the direction normal to the wall.

Recently, Mashayek[8] (1998) used DNS, with 96^3 grid points, to study droplet–turbulence interactions in a homogeneous shear flow. He considered both one-way and two-way couplings for nonevaporating and evaporating droplets. He showed that in the case of nonevaporating droplets, the turbulence kinetic energy is reduced and the flow anisotropy is increased due to the two-way coupling. In the case of evaporating droplets he found that the turbulence kinetic energy and the mean internal energy of the carrier flow are increased by mass transfer. Unfortunately, the study of Mashayek[8] is of purely parametric nature and does not discuss the physical reasons for the observed changes in turbulence due to the particles.

The objective of the present paper is to answer the question: What are the physical mechanisms responsible for the modification of the turbulence structure by solid particles dispersed in a homogeneous shear flow? In our simulations, we use DNS to study the effects of dispersed solid particles on turbulence structure in a homogeneous turbulent shear flow. We observe a reduction as well as an increase in the turbulence kinetic energy of the carrier flow under different conditions, and we provide, for the first time, an explanation of the physical mechanisms responsible for these modifications. Moreover, we consider the role played by gravity which was not considered by Mashayek.[8]

Our results show that dispersed particles modify the turbulence structure via changing the turbulence energy production rate. The change in the turbulence energy production rate is caused by the modification of the vorticity dynamics. It is known that regions of large turbulence production rate are sandwiched between counter rotating longitudinal vortex tubes (Adrian an Moin[9] and Kida and Tanaka[10]). The stronger the vorticity, ω_s, of these longitudinal vortex tubes is, the larger the production rate. The dispersed solid particles modify the alignment of the vorticity vector, $\boldsymbol{\omega}$, with the axis of the longitudinal vortex tube. Increasing the alignment between the vorticity vector and the axis of the longitudinal vortex tube increases ω_s, which in turn increases the turbulence production rate, and vice versa.

The paper is organized as follows. In Sec. II, the governing equations are discussed. The results are presented in Sec. III. Turbulence and particles parameters are presented in Sec. III A. Turbulence modification by the particles are discussed in Sec. III B. The mechanisms of modification of turbulence energy production by the particles are introduced in Sec. III C. The effect of particles on modifying the alignment between vorticity and strain eigenvectors are shown in Sec. III E. A summary of the findings of this paper is presented in Sec. IV.

II. MATHEMATICAL DESCRIPTION

The study of the two-way coupling between the particles and fluid requires the simultaneous solution of the Navier–

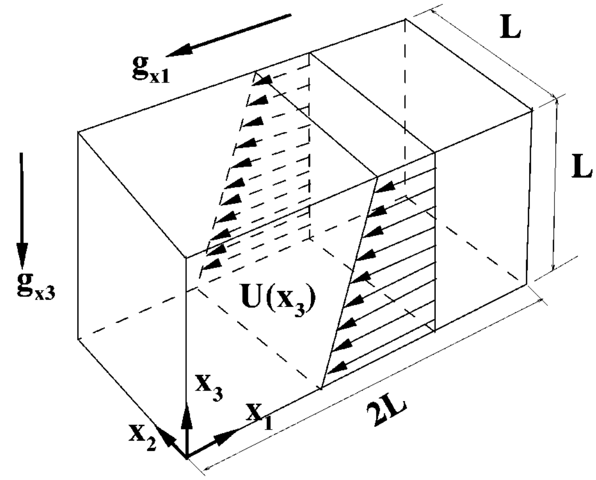

FIG. 1. Schematic of flow configuration.

Stokes and continuity equations that describe the time evolution of the flow field, plus the dynamic equation that describes the particle motion. The dimensionless Navier–Stokes and continuity equations for a homogeneous shear flow are:

$$\frac{\partial u_i}{\partial t}+\frac{\partial}{\partial x_j}(u_j u_i)+Sx_3\frac{\partial u_i}{\partial x_1}+Su_3\delta_{i1}=\frac{1}{\mathrm{Re}}\frac{\partial^2 u_i}{\partial x_j^2}-\frac{\partial p}{\partial x_i}-f_i, \tag{1}$$

$$\frac{\partial u_i}{\partial x_i}=0, \tag{2}$$

where $i=1,2,3$ refer to the three space directions x_1,x_2,x_3. f_i is the force that represents the effect of the M particles that are within the fluid integration cell, and is calculated from

$$f_i=\frac{1}{m_f}\sum_{k=1}^{M} f_{ik}, \tag{3}$$

where f_{ik} is the drag force on particle k, see Eq. (5) below, in x_i direction. m_f is the mass of the fluid in the integration cell. An expression for f_i is derived in the Appendix. For one-way coupling flows f_i is zero. $u_i(t)$ is the deviation of the instantaneous fluid velocity $\tilde{u}_i(t)$ from the imposed mean velocity ($U=Sx_3$) according to

$$u_i=\tilde{u}_i-(Sx_3)\delta_{i1}, \tag{4}$$

where S is the dimensionless mean velocity gradient, given by $S=(dU/dx_3)(L/\Delta U)=1$ in our simulations. ΔU is the difference between the mean velocities at the top and bottom boundaries of the computational domain (Fig. 1). L is the computational domain length which equals unity in the vertical and spanwise directions, and equals two in the streamwise direction to allow for the growth of the integral length scale without violating the periodicity boundary condition in that direction. It should be noted that since the particles volume fraction is small, $\phi_v<10^{-3}$, we neglect the effect of the presence of the particles on the continuity equation (2) of the carrier fluid.

The equation that describes the particle motion is that derived by Maxey and Riley[11] and which for large particle–fluid density ratio can be written as

$$m_p(dv_i/dt_p)=m_p(u_i-v_i)/\tau_p-m_p[d(Sx_3)/dt_p]\delta_{i1}+(m_p-m_f)g_i, \tag{5}$$

where $v_i(t)$ is the deviation of the instantaneous particle velocity $\tilde{v}_i(t)$ in x_i direction from the local mean fluid velocity

$$v_i=\tilde{v}_i-(Sx_3)\delta_{i1}, \tag{6}$$

d/dt_p is the time derivative following the moving particle, and τ_p is the particle response time, which for Stokes flow reads

$$\tau_p=\frac{2\rho_p a^2}{9\rho v}, \tag{7}$$

where a is the particle radius; ρ_p is the particle density, and ρ is the fluid density.

The flow field governing equations are discretized in an Eulerian framework using a second-order accurate Adams–Bashforth scheme for time integration on a staggered grid containing 160×80×80 grid points. This grid allows an initial microscale Reynolds number of $R_{\lambda,0}=20$. The pressure is treated implicitly by solving the Poisson equation in finite difference form using a Fast Fourier Transform (FFT). The boundary conditions are periodic in the x_1 and x_2 directions and shear periodic in the x_3 direction. The shear periodic boundary condition for any variable $f(t,x_1,x_2,x_3)$ is prescribed as

$$f(t,x_1+m_1,x_2+m_2,x_3+m_3)=f(t,x_1-Sm_3t,x_2,x_3), \tag{8}$$

where m_i are integer numbers. More detailed description of the solution procedure is given by Gerz *et al.*[12]

The initial turbulent velocity field is isotropic, periodic in the three directions and divergence free. This flow is allowed to develop until the skewness of the velocity derivative ≈ -0.45, then a constant mean velocity gradient is imposed on the flow. The initial energy spectrum, $E(k,0)$, is prescribed by

$$E(k,0)=16(2/\pi)^{1/2}(3/2)u_0^{*2}\frac{k^4}{k_p^5}\exp(-2(k/k_p)^2), \tag{9}$$

where k_p is the wave number at which the maximum of the energy spectrum occurs, and u_0^* is the initial root-mean-square velocity. All the wave numbers appearing in (9) are normalized by 2π. Equation (9) produces an energy spectrum with most of the energy content confined in wavenumbers surrounding k_p. This spectrum allows us to increase the duration of the simulation without violating the periodicity boundary condition in the streamwise direction. Specifying u_0^* and k_p are sufficient to calculate $E(k,0)$. The initial dimensionless kinematic viscosity v is calculated from the initial prescribed Reynolds number $R_{\lambda,0}$ and computed initial energy dissipation rate ϵ_0. The values of the initial dimensionless parameters used in our simulation are shown in Table I.

TABLE I. Dimensionless flow parameters at $T=0$. η_0 is the initial Kolmogorov length scale and l_0 is the initial integral length scale.

R_λ	20.0
$k_p/2\pi$	5.0
u_0^*	0.035 30
v_0	0.000 1050
ϵ_0	0.000 5546
l_0	0.072 980
λ_0	0.059 510
η_0	0.006 761
$\eta k_{\max}$	1.699

Since the mean velocity gradient (dU/dx_3) is constant and is set equal to unity, we use its inverse as a reference time $T_{\mathrm{ref}}=1$, which results in a reference length $L_{\mathrm{ref}}=0.390\,36$ m.

In order to ensure that our DNS resolves the motion at the smallest scales we monitor the values of the dimensionless quantity $\eta k_{\max}$, where $k_{\max}$ is the highest resolved wave number $[=2\pi(N/2)]$. N is the number of grid points in a given direction. In our simulations $1.6\leqslant\eta k_{\max}\leqslant 1.8$ for $1\leqslant T\leqslant 6$. Moreover, we ensure that the two point Eulerian velocity autocorrelation in the x_1 direction diminishes to zero in less than half the length of the computational domain. In order to satisfy this criterion we extend the computational domain in the streamwise direction to twice its size in the lateral directions.

The particle equation of motion is integrated in time using a second-order accurate Adams–Bashforth scheme to obtain the particle velocity. The fluid velocity at the particle position is obtained using a fourth-order accurate, two-dimensional, four-point, Hermitian cubic interpolation scheme,(Truesdell[13]). The particle position is obtained by integrating the particle velocity in time. The boundary conditions for the particle equation are periodic in the x_1 and x_2 directions and shear periodic in the x_3 direction.

In order to calculate the number of computational particles required for a given volume fraction for the two-way coupling and avoid excessive computational time, we assume that each computational particle represents a maximum of 45 real particles. Elghobashi and Truesdell[5] showed that the DNS results using one computational particle to represent about 100 actual particles are within 2% of that is produced using half of that number. Particles are injected in the flow at $T=1$ at which time the skewness of the velocity derivative reaches its first peak, thus signifying fully developed turbulence. The prescribed initial particle velocity is the same as that of the surrounding fluid at the point of injection.

III. RESULTS

A. Turbulence and particles parameters

In our simulations of the two-way interaction between particles and a homogeneous turbulent shear flow we studied five different cases. The properties of the particles in these cases are shown in Table II. Case A represents a particle-free flow with which other cases are compared. Cases B and C study the effect of increasing particle inertia or response

TABLE II. Particle parameters at injection, $T=1$. Dimensionless quantities (τ_p and d) are normalized by a reference time=1 s and a reference length=0.390 36 m. $\mathrm{Sh}=Sl_0/u_0^*$ is the shear number.

Case	Sh	τ_p	d	ρ_p/ρ	τ_p/τ_e	τ_p/τ_K	d/η	ϕ_v	ϕ_m	v_t/u_0^*	g_{x_i}
A	2							0.0	0.0		
B	2	1.0	1.0×10^{-3}	1890	0.4140	2.330	0.1479	5.0×10^{-4}	1.0	0.0	
C	2	0.10	6.0×10^{-4}	525	0.0414	0.233	0.0887	1.9×10^{-4}	0.1	0.0	
D	2	0.10	6.0×10^{-4}	525	0.0414	0.233	0.0887	1.9×10^{-4}	0.1	1.59	x_1
E	2	0.10	6.0×10^{-4}	525	0.0414	0.233	0.0887	1.9×10^{-4}	0.1	1.59	x_3

time, τ_p. The particles mass loading in case B equals one; i.e., one order of magnitude larger than that of case C. The effect of gravity is studied in cases D (gravity in $-x_1$ direction) and E (gravity in $-x_3$ direction).

B. Turbulence modification by particles

In this subsection we discuss the effect of two-way coupling on modifying the structure of turbulence for cases B–E listed in Table II. We have performed 10 simulations of which we selected these four cases. Careful examination of our results showed that these four cases are sufficient to explain the physical mechanisms that are responsible for modifying the structure of the turbulent homogeneous shear flow by dispersed solid particles. In Sec. III D, we present the results of all the ten simulations in a parametric form that shows the effects of varying the mass loading, particle inertia and drift velocity.

Figure 2 shows the time development of the turbulence kinetic-energy $E(T)$ and its rate of dissipation $\epsilon(T)$ normalized by their initial values for cases A (no particles), B and C. It should be noted that, due to the particles small inertia and mass loading of case C, the two-way coupling effects are small. The figure shows that for times $T>2$, the particles reduce $E(T)$ for case B relative to A, whereas they increase it in case C. The reasons for this different behavior will be discussed in the next paragraph. The rate of turbulence dissipation, $\epsilon(T)$, increases in both cases with case B having the largest initial increase. However, near the end of simulation where the turbulence energy of the coupled flow in case B becomes substantially smaller than that of case A (the uncoupled flow), the rate of dissipation of turbulence energy, $\epsilon(T)$, of case B becomes smaller than that of case A. Continuing the simulation for $T>6$ would result in a significantly weaker turbulence, since R_λ of case B declines to 13.8 at that time, and thus we terminate all simulations at $T=6$. The temporal behavior of the three components of turbulence kinetic energy is displayed in Fig. 3 where it is clear that, relative to case A, all three components of the root-mean-square (rms) velocities are reduced in case B, while they tend to increase in case C, especially in the x_1 direction (the other two directions show a negligible change). It should be noted that in case B, although the reduction in $u_{2,\mathrm{rms}}$ is the largest compared to the other two components, the relative reduction in $u_{i,\mathrm{rms}}$, $i=2,3$ is almost the same (the relative reduction in $u_{2,\mathrm{rms}}$ at $T=6$ is 33%, while it is 29% for $u_{3,\mathrm{rms}}$ at the same time) as expected for particles in zero gravity. The reason for the largest reduction in $u_{2,\mathrm{rms}}$ will be discussed later on in this section.

In order to understand the reason for the above mentioned modifications of the turbulence energy, we consider the transport equation for turbulence energy for a turbulent

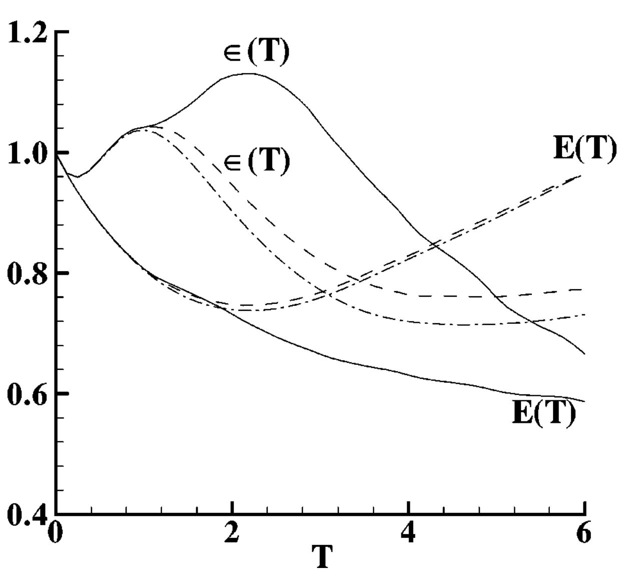

FIG. 2. Time development of $E(T)$ and its rate of dissipation $\epsilon(T)$. Case B (solid lines), case C (dashed lines), case A (dash–dot lines).

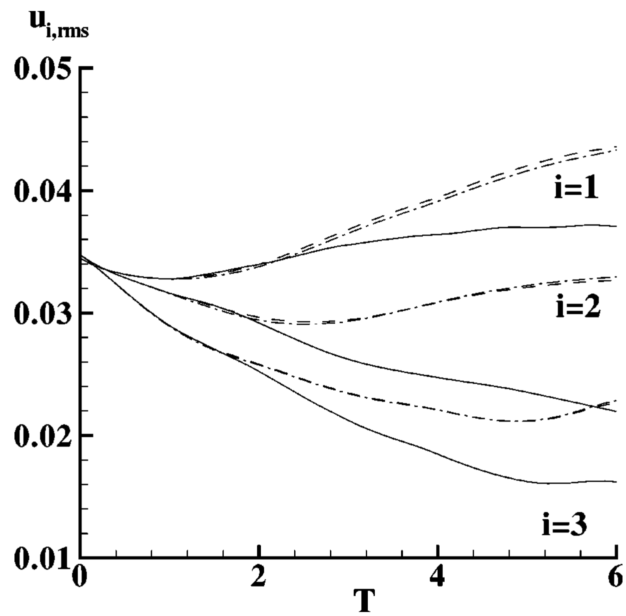

FIG. 3. Time development of rms velocity components. Case B (solid lines), case C (dashed lines), case A (dash–dot lines).

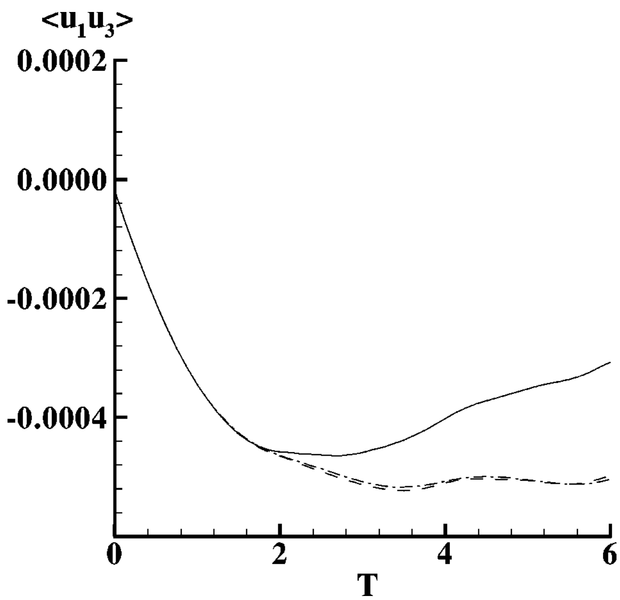

FIG. 4. Time development of the velocity correlation, $\langle u_1 u_3 \rangle$. Case B (solid lines), case C (dashed lines), case A (dash–dot lines).

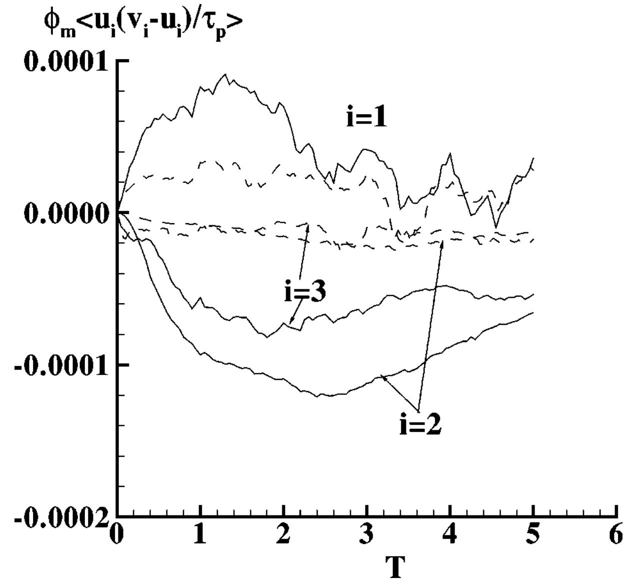

FIG. 5. Time development of the particles source term in the x_i directions. Case B (solid lines), case C (dashed lines).

homogeneous shear flow laden with particles. This equation can be derived from Eq. (1) by multiplying throughout by u_i and ensemble averaging to obtain

$$\frac{dE(t)}{dt} = -S\langle u_1 u_3 \rangle - \epsilon + S_p, \tag{10}$$

where the first term on the right-hand-side (RHS) of (10) is the rate of turbulence production by mean shear; the second term is the rate of turbulence viscous dissipation, and the third term, S_p, is the source term due to the particles which, for particles in zero gravity, is given by

$$S_p = -\phi_m \langle u_i (u_i - v_i)/\tau_p \rangle, \tag{11}$$

The increase in the rate of turbulence energy dissipation, $\epsilon(T)$, shown in Fig. 2 is one factor that reduces the turbulence energy. The effect of the other two terms on the RHS of (10) are discussed next.

Figure 4 shows the time development of $\langle u_1 u_3 \rangle$ for cases A–C. Since $S=1$ in our flow, the time rate of change of $-\langle u_1 u_3 \rangle$ represents the rate of production of turbulence energy by the mean shear. The figure shows that the magnitude of the rate of production of turbulence energy by mean shear is reduced in case B relative to case A, while it is slightly increased in case C with a tendency to decrease near the end of the simulation. This modification of the rate of energy production is consistent with the modification of the turbulence energy shown in Fig. 2. In Sec. III C we will show that the change of the alignment between the vorticity vectors and their longitudinal vortex tubes is the physical mechanism responsible for this modification of the turbulence energy production rate.

The RHS of Eq. (11) shows that the magnitude of S_p depends on the correlation between the fluid and particles velocities, u_i and v_i. Figure 5 shows the time development of the components of the source term S_p in x_i directions for cases B and C. It is seen that this term is a source of energy in the x_1 direction in both cases, while it is a sink of energy in the other two directions. Due to the imposed mean velocity gradient and the initial condition of equal local velocities of particle and fluid, and due to particle inertia, the particle velocity in the x_1 direction becomes larger than that of the fluid. Thus the particles are able to align the fluid velocity along their direction of motion, resulting in higher $\langle u_1 v_1 \rangle$ correlation than that of the energy component $\langle u_1 u_1 \rangle$ as seen in Fig. 6 for case B. In the other two directions (x_2, x_3), there is no mean velocity gradient and thus the particles lag the fluid, resulting in $\langle u_i v_i \rangle$ being smaller than $\langle u_i u_i \rangle$ in these directions. The temporal developments of the components of S_p, shown in Fig. 5, help explain the changes in the rms velocity components in Fig. 3. The reduction of $u_{2,\mathrm{rms}}$

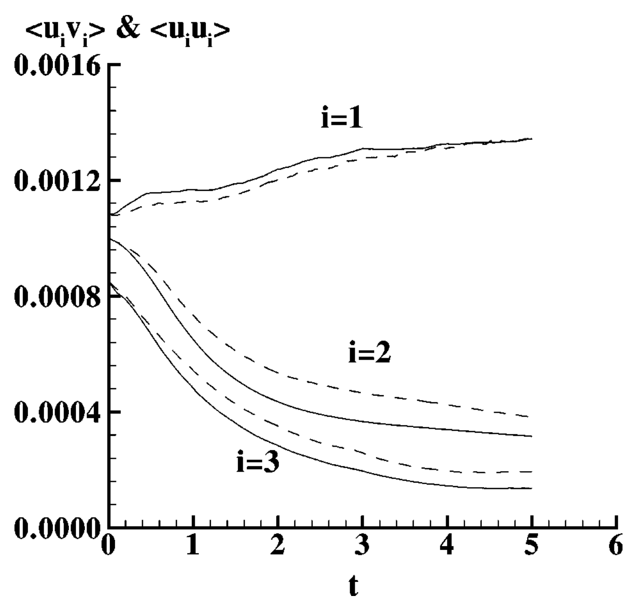

FIG. 6. Time development of $\langle u_i v_i \rangle$ (solid lines) and $\langle u_i u_i \rangle$ (dashed lines) of case B.

of case B being larger than that of $u_{1,\mathrm{rms}}$ and $u_{3,\mathrm{rms}}$ is consistent with that of the x_2 component of S_p of case B, having the largest negative value compared to the other two directions. The positive source term of case B in the x_1 direction does not result in an increase in its $u_{1,\mathrm{rms}}$, indicating that the reduction in $u_{1,\mathrm{rms}}$ of case B is mainly due to the reduction in the production rate of turbulence energy seen in Fig. 4.

The spectral equation of energy $E(K_i)$ can be obtained from the momentum equation (1) by Fourier transformation, resulting in

$$\frac{\partial E(K_i)}{\partial t}=A(K_i)+G(K_1)+T(K_i)+P(K_i)+\epsilon(K_i)+F(K_i) \quad i=1,2,3, \tag{12}$$

where $A(K_i)$ is the linear energy transfer rate due to the mean shearing deformation of the turbulent eddies (Domaradzki *et al.*[14] and Deissler[15]), $G(K_1)$ is the turbulence energy production rate, $T(K_i)$ is the nonlinear energy transfer rate across the wave number space, $P(K_i)$ is the rate of energy transfer by velocity pressure-gradient correlation, $\epsilon(K_i)$ is the rate of energy dissipation, and $F(K_i)$ is the rate of energy gain (or loss) due to the two-way coupling which equals the spectrum of correlation between the net particle acceleration and local fluid velocity. The equations for the components on the RHS of Eq. (12) are

$$G(K_1)=-\tfrac{1}{2}S(\hat{u}(K_1)\overline{\hat{u}(K_3)}+\overline{\hat{u}(K_1)}\hat{u}(K_3)), \tag{13}$$

$$\begin{aligned}T(K_i)=\frac{i}{2}\{&\hat{u}(K_i)[\overline{\hat{u}(K_1)}*(K_1\overline{\hat{u}(K_i)})]-\overline{\hat{u}(K_i)}[\hat{u}(K_1)*(K_1\hat{u}(K_i))]+\hat{u}(K_i)[\overline{\hat{u}(K_i)}*(K_2\overline{\hat{u}(K_i)})]\\&-\overline{\hat{u}(K_i)}[\hat{u}(K_2)*(K_2\hat{u}(K_i))]+\hat{u}(K_i)[\overline{\hat{u}(K_3)}*(K_3\overline{\hat{u}(K_i)})]-\overline{\hat{u}(K_i)}[\hat{u}(K_3)*(K_3\hat{u}(K_i))]\},\end{aligned} \tag{14}$$

$$\begin{aligned}A(K_i)=\frac{i}{2}S[&\hat{u}_i(\overline{\hat{x}_3}*(k_1\overline{\hat{u}(K_i)}))\\&-\overline{\hat{u}(K_i)}(\hat{x}_3*(K_1\hat{u}(K_i)))],\end{aligned} \tag{15}$$

$$P(K_i)=\frac{i}{2}\{\hat{u}(K_i)(K_i\overline{\hat{p}})-\overline{\hat{u}(K_i)}(K_i\hat{p})\}, \tag{16}$$

$$\begin{aligned}\epsilon(K_i)=\frac{-1}{2\,\mathrm{Re}}\{&\hat{u}(K_i)(K_1^2+K_2^2+K_3^2)\overline{\hat{u}(K_i)}\\&+\overline{\hat{u}(K_i)}(K_1^2+K_2^2+K_3^2)\hat{u}(K_i)\},\end{aligned} \tag{17}$$

$$F(K_i)=\frac{-1}{2}\{\hat{u}(K_i)\overline{\hat{f}(K_i)}+\overline{\hat{u}(K_i)}\hat{f}(K_i)\}, \tag{18}$$

where the quantities with over bar denote complex conjugate, ''$*$'' denotes complex convolution, ''$\wedge$'' denotes Fourier transform. For a detailed derivation of (12) the reader is referred to Ahmed.[16]

The spectral distributions of the three-dimensional turbulence kinetic-energy $E(K)$ and its rate of dissipation $\epsilon(K)$ at $T=4$ are shown in Fig. 7 for case B. It is clear that both $E(K)$ and $\epsilon(K)$ are increased at large wave numbers and reduced at small wave numbers. The net effect is a reduction in turbulence kinetic energy and an increase in rate of turbulence dissipation. The increase in turbulence energy at large wave numbers is due to the increase in the nonlinear energy transfer, $T(K)$, from small wave numbers to large wave numbers. The reduction in turbulence kinetic energy at small wave numbers of case B is directly related to the reduction in the rate of turbulence energy production as seen in Fig. 8. In addition, turbulence energy is reduced at small wavenumbers due to particles drag.

Now, we discuss the combined effect of the two-way coupling and gravity on the turbulence structure. Figure 9 shows $E(T)$ and $\epsilon(T)$ for cases A (no particles), D (coupled flow with gravity in $-x_1$ direction) and E (coupled flow with gravity in $-x_3$ direction). It is clear that the effect of gravity in the $-x_1$ direction is to substantially increase both $E(T)$ and $\epsilon(T)$ compared to the particle-free flow, A. On the other hand, for case E (gravity imposed in the $-x_3$ direction), Fig. 9, shows higher rates of increase in $E(T)$ and $\epsilon(T)$ till $T\approx 2.5$ for $E(T)$ and $T\approx 3.5$ for $\epsilon(T)$ after which the trend is reversed. The effect of gravity direction is further manifested in Fig. 10, where the rate of turbulence production is higher in case E than that of case D for $T>2$ and both rates become nearly equal near the end of the simulation. In Sec. III C we

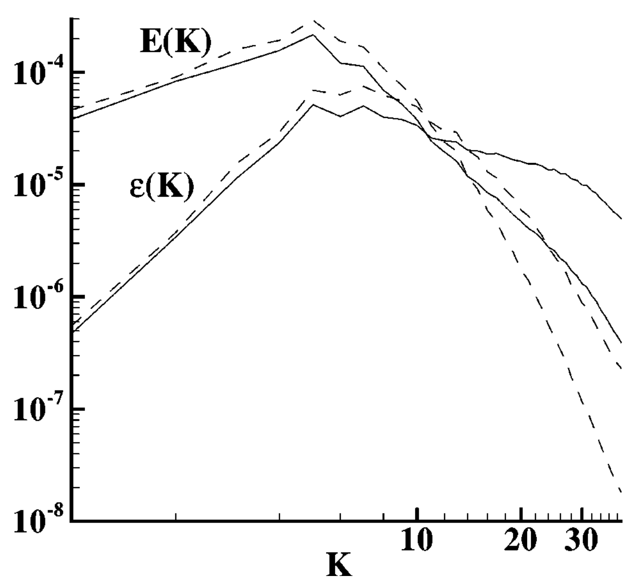

FIG. 7. Three-dimensional spectrum distribution of turbulence kinetic-energy $E(K)$, and its rate of dissipation $\epsilon(K)$, at $T=4$. Case B (solid lines), case A (dashed lines).

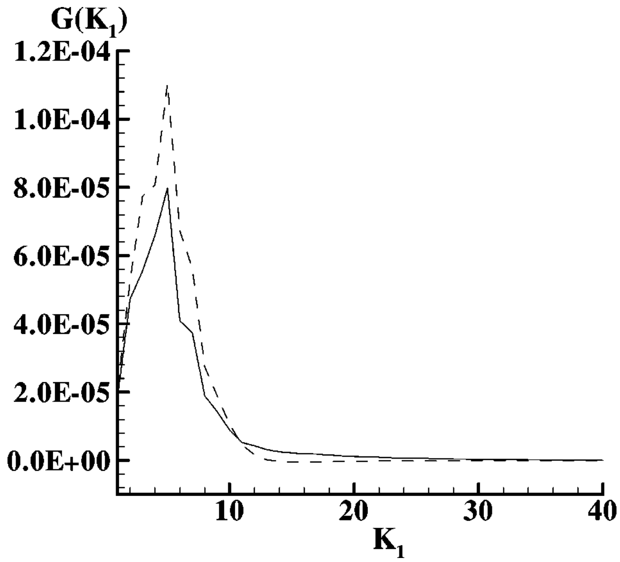

FIG. 8. Spectrum of energy production $G(K_1)$ at $T=4$. Case B (solid lines), case A (dashed lines).

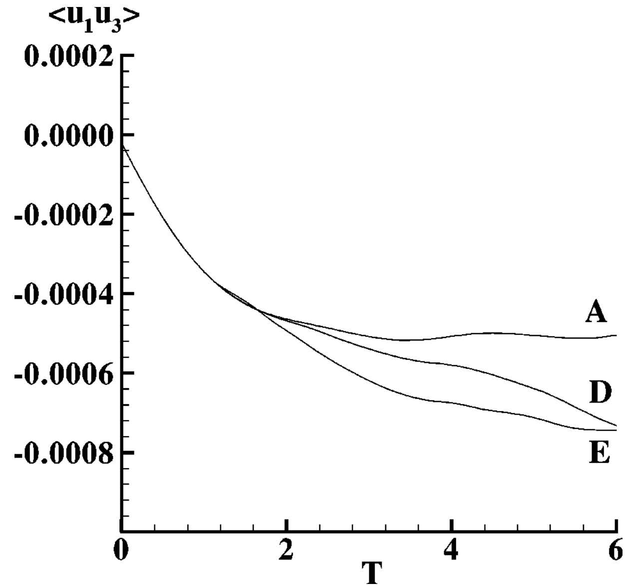

FIG. 10. Time development of the velocity correlation, $\langle u_1 u_3\rangle$.

will show that the change in the alignment between the vorticity vectors and their longitudinal vortex tubes is the physical mechanism responsible for this modification in turbulence energy production rate.

The temporal development of the root-mean-square velocity components, $u_{i,\mathrm{rms}}$, for cases A, D, and E are shown in Fig. 11. It is clear that the increase of energy is nonisotropic with most of the increase occurring in the direction of gravity. It is also clear that the increase in turbulence energy in cases D and E (Fig. 9) is not only due to the increase in the turbulence production rate but also due to the transfer of energy from the particles, that have higher energy in the gravity direction, to the fluid via the drag. This argument can be clarified by considering the coupling source term. The source term in the fluid equation of motion [Eq. (1)], $(-f_i)$ can be written as (see the Appendix)

$$-f_i=\frac{\rho_p}{\rho}\overline{\phi_v} g\,\delta_{ik}-\frac{\rho_p}{\rho}\phi_v g\,\delta_{ik}-\frac{\rho_p}{\rho}\phi_v\frac{d\tilde{v}_i}{dt}. \tag{19}$$

The first term on the RHS of (19) is constant and its effect is to balance the mean drift caused by the particles. The second term is the particles source term due to gravity. The third term is an additional source term due to particles inertia. When the particle is moving with its terminal velocity, its acceleration, $d\tilde{v}_i/dt$, in the direction of gravity becomes either negligible in case E or becomes $-(\rho_p/\rho_f)\phi_v S v_3$ in case D. Hence, the particle's source term in the direction of gravity is mainly $-(\rho_p/\rho_f)\phi_v g$ in both cases. Obviously,

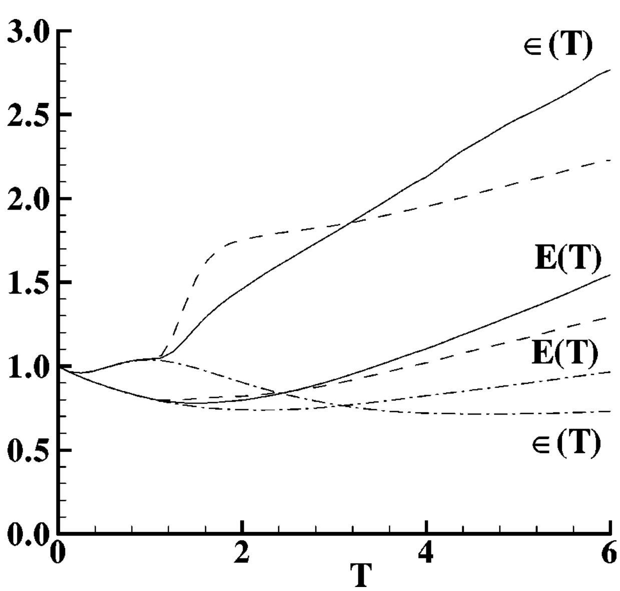

FIG. 9. Time development of $E(T)$ and its rate of dissipation $\epsilon(T)$. Case D (solid lines), case E (dashed lines), case A (dash–dot lines).

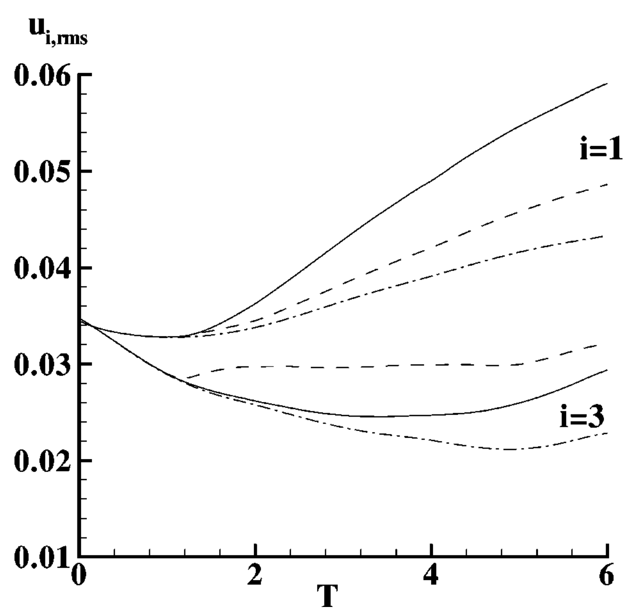

FIG. 11. Time development of rms velocity components. Case D (solid lines), case E (dashed lines), case A (dash–dot lines).

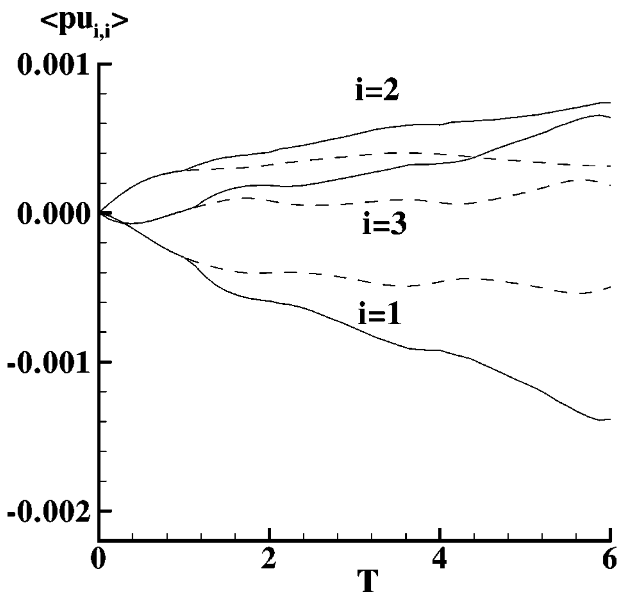

FIG. 12. Time development of pressure strain correlation $\langle pu_{i,i}\rangle$. Case D (solid lines), case A (dashed lines).

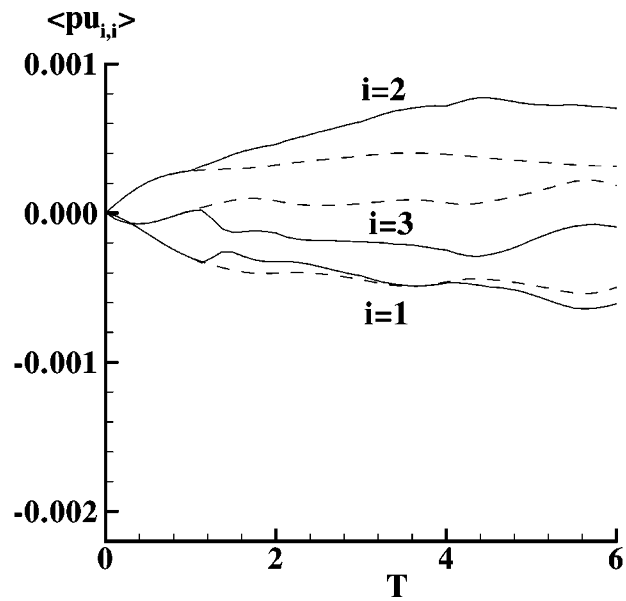

FIG. 13. Time development of pressure strain correlation $\langle pu_{i,i}\rangle$. Case E (solid lines), case A (dashed lines).

this force will cause the fluid to drift along the direction of particles motion. Thus, the fluid velocity will be positively correlated with this force, i.e., $-u_i(\rho_p/\rho_f)\phi_v g\delta_{ik}$ will be positive on average. The additional source term in case D, $-(\rho_p/\rho_f)\phi_v S v_3$, is responsible for the higher turbulence level of case D compared to case E after $T \approx 2.5$ in Fig. 9.

Turbulence energy produced by the mean shear and particles–turbulence interaction in the gravity direction is transferred to the lateral directions by pressure-strain correlations, $\langle pu_{i,i}\rangle$. Figures 12 and 13 show the time development of $\langle pu_{i,i}\rangle$ for cases A, D, and E. Figure 12, shows that imposing gravity in the direction of the mean velocity enhances the role of $\langle pu_{i,i}\rangle$, i.e., more energy is transferred from the x_1 direction to the lateral directions x_2 and x_3. On the other hand, when gravity is imposed in the $-x_3$ direction, the pressure-strain correlation causes energy to be transferred from the x_3 direction to the x_2 direction and slightly to the x_1 direction until $T \approx 3$. As turbulence energy production by shear increases the pressure strain correlation $\langle pu_{1,1}\rangle$ causes more energy to be transferred from the x_1 direction to the x_2 direction for $T > 3$.

C. Mechanisms of modification of turbulence energy production by the particles

1. Creation of local velocity gradients

When particles at a relatively small volume fraction $\phi_v \approx O(10^{-3})$, are injected with a spatially uniform distribution in a homogeneous turbulent shear flow, they create local velocity gradients. The creation of local velocity gradients can be explained by reference to Fig. 14. The figure shows particles moving with a uniform velocity in a certain direction encountering a clockwise vortex. If the velocity of the solid particles is *larger* than that of the surrounding fluid, the drag between the solid particles and fluid will increase the velocity of the fluid which was initially moving in the same direc-

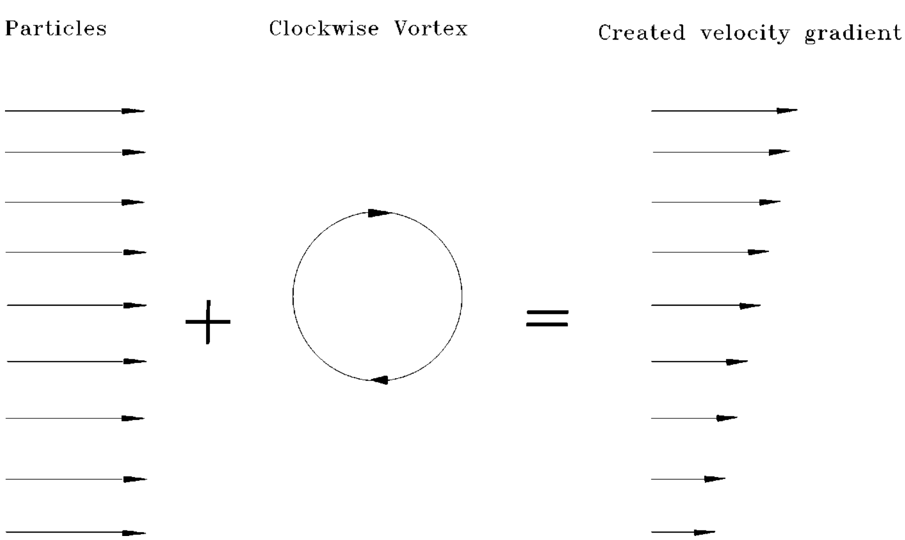

FIG. 14. Local velocity gradient in the carrier flow created by the interaction of particles with a vortex.

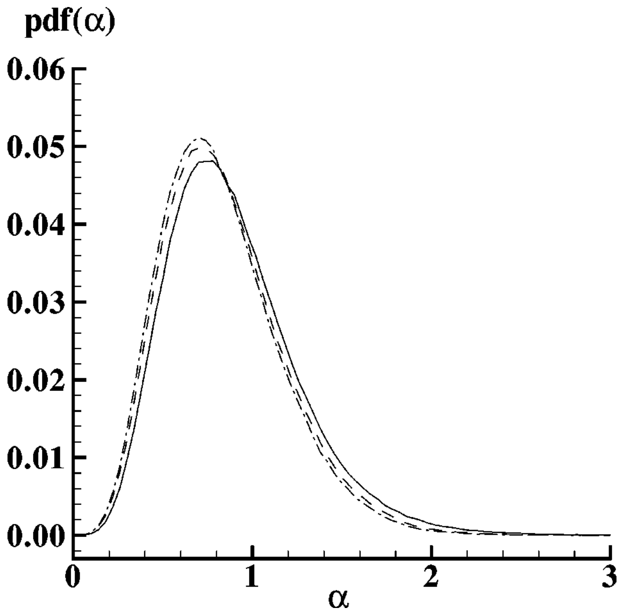

FIG. 15. pdf of α strain eigenvalue at $T=3$. Case B (solid lines), case C (dashed lines), case A (dash–dot lines).

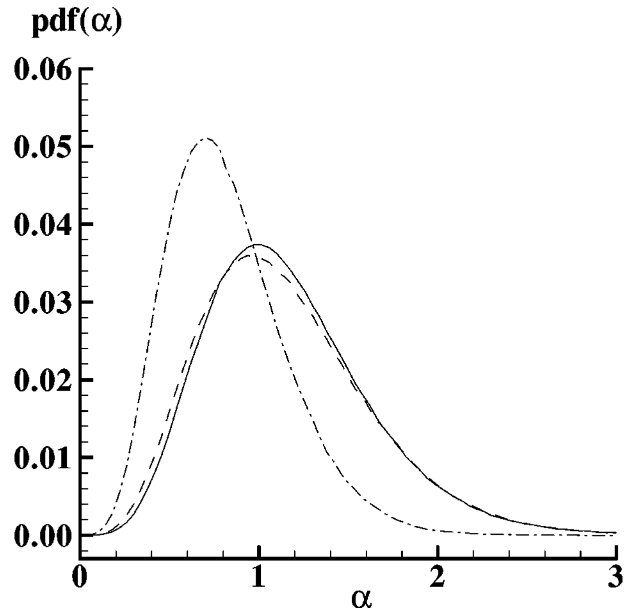

FIG. 16. pdf of α strain eigenvalue at $T=3$. Case D (solid lines), case E (dashed lines), case A (dash–dot lines).

tion of the particles. The fluid that was moving opposite to the solid particles will experience a velocity reduction. The net effect of this interaction is the creation of the velocity gradient seen in Fig. 14. On the other hand, if particles are slower than the surrounding fluid, they will reduce the fluid velocity everywhere. However, the fluid points that were moving in the direction of the particles will experience smaller reduction in their velocity than those opposing the particles motion, thus creating a local velocity gradient similar to that in Fig. 14. This creation of local velocity gradients leads to an increase in the magnitude of the local strain rate, thus increasing the dissipation rate of turbulence kinetic energy of the coupled flow compared to the uncoupled flow as discussed in the previous subsection. The increase in the dissipation rate is manifested in the increase in the strain rate eigenvalues α (the extensional strain), β (the intermediate strain), and γ (the compressive strain). The strain rate tensor eigenvalues are related to the square of the strain tensor, and hence dissipation, through the relations

$$S_{ij}=(u_{i,j}+u_{j,i})/2, \tag{20}$$

$$S_{ij}S_{ij}=\alpha^2+\beta^2+\gamma^2, \tag{21}$$

$$\epsilon=2\upsilon S_{ij}S_{ij}. \tag{22}$$

Figure 15 shows the probability density distribution of α eigenvalue at $T=3$, and indicates an increase in its magnitude in cases B and C as compared to case A. This increase can be seen by comparing the amplitudes of the pdf(α) for large values of α. It is clear that cases B and C have larger amplitudes for large α than that of case A. The increase in the α eigenvalue for cases D and E as compared to case A at $T=3$ is shown in Fig. 16. It is seen that the increase of the magnitude of the eigenvalue is proportional to the changes in the dissipation rate seen in Figs. 2 and 9 at $T=3$. It should be noted that the eigenvalues β, and γ of the coupled cases also increase (figures are not shown).

As the flow develops, solid particles tend to accumulate in regions of low vorticity (high strain), (Wang and Maxey[17]). This accumulation is quantified by calculating the time development of the quantity D_c which measures the sum of the squared difference between the actual probability of concentration of particles and the probability of random distribution (Wang and Maxey[17])

$$D_c=\sum_{C=0}^{N_p}(P_c(C)-P_c^u(C))^2, \tag{23}$$

where N_p is the total number of particles and represents the maximum value that can be assigned to C. The random distribution probability function $(P_c^u(C))$ is calculated from

$$P_c^u(C)=\binom{N_p}{C}\left(\frac{1}{N_g}\right)^C\left(1-\frac{1}{N_g}\right)^{N_p-C},$$
$$C=0,1,2,\ldots,N_p, \tag{24}$$

where

$$\binom{N_p}{C}=\frac{N_p(N_p-1)\cdots(N_p-C+1)}{C!}, \tag{25}$$

and N_g is the number of grid points in the computational domain. Figure 17 shows the temporal development of D_c for case B. It is seen that D_c gradually increases until $T=3$, then it varies slowly for $T>3$, signifying a slower rate of accumulation. The slower rate of accumulation after $T=3$ is due to the decrease in turbulence energy as seen in Fig. 2. This preferential accumulation of particles, which is largest when the particle response time is equal to the Kol-

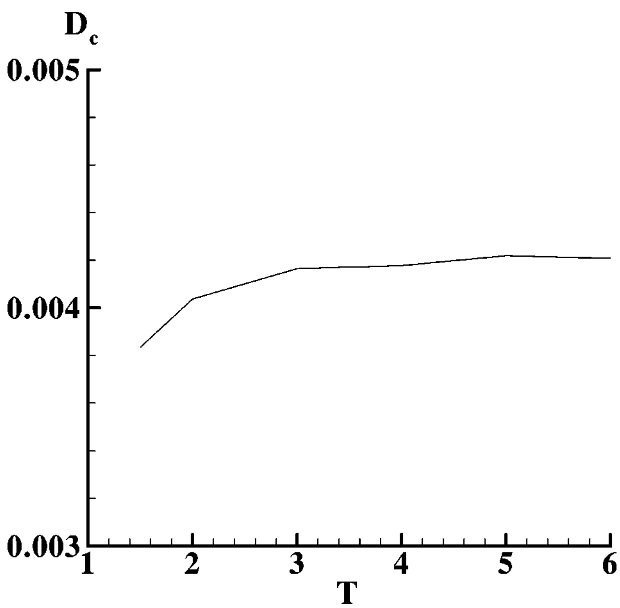

FIG. 17. Time development of D_c of case B.

mogorov time scale, leads to a further increase of the local velocity gradients of the surrounding fluid, which in turn modifies the vorticity dynamics.

2. Modification of vorticity dynamics

Consider the vorticity transport equation which is obtained by taking the curl of the momentum equation (1)

$$\frac{\partial \omega_i}{\partial t}=\left(-Sx_3\frac{\partial \omega_i}{\partial x_1}-u_k\frac{\partial \omega_i}{\partial x_k}\right)+\left(S\omega_3\delta_{i1}-S\frac{\partial u_i}{\partial x_2}+\omega_k\frac{\partial u_i}{\partial x_k}\right)$$
$$+\upsilon\frac{\partial^2 \omega_i}{\partial x_k^2}+b_i \quad (i=1,2,3), \tag{26}$$

where ω_i are the fluctuating vorticity components, and b_i is the curl of the two-way coupling force term in Eq. (1)

$$b_i=-\epsilon_{ijk}\frac{\partial f_k}{\partial x_j}. \tag{27}$$

The two terms in the first bracket on the RHS of (26) represent vorticity advection by both the mean velocity (due to mean shear) and fluctuating velocity respectively, without changing the direction of ω_i. It should be noted that these two terms advect the vorticity vectors and vortical structures at the same rate. The first term in the second bracket converts the vertical component of vorticity, ω_3, to the horizontal component, ω_1, by mean shear. The second term in the second bracket converts the mean vorticity, $-S$, to ω_1 and ω_3 components for $i=1,3$ respectively, and stretches the mean vorticity for $i=2$. The third term in the second bracket converts the vorticity from ω_k to ω_i, $i\neq k$, i.e., it changes the vorticity direction. The term $\upsilon\,\partial^2\omega_i/\partial x_k^2$ is the viscous diffusion of vorticity. The last term represents a source/sink of vorticity due to the solid particles.

Kida and Tanaka[18] studied numerically the temporal development of the vorticity field in homogeneous turbulent shear flows. They indicated that the imposed mean shear stretches a randomly distributed initial vorticity field into longitudinal vortex tubes (elongated high vorticity regions) that are initially inclined at 45° to the downstream. These elongated vortex tubes become more inclined toward the mean-stream direction as the flow develops in time. The elongated vortex tubes induce a strong swirling motion around them. The term $(-S\partial u_i/\partial x_2)$ in Eq. (26) which converts the mean vorticity $(-S)$ into the direction of the spanwise derivative of the induced velocity vector $(\partial \mathbf{u}/\partial x_2)$, begins to take part in the dynamics. Figures 18(a) and 18(b) show two longitudinal vortex tubes with the vorticity vectors represented by solid arrows along their centerline for positive and negative vorticities, respectively. The velocity **u** induced by these vortices is shown by curved arrows around the longitudinal vortex tubes. The spanwise derivative of this induced velocity is in the direction of **u**, and is denoted by the bold arrows, i.e., it is in the same direction as that of the induced velocity. Thus, due to $(-S\partial u_i/\partial x_2)$, the vorticity vectors move away from the centerlines of the longitudinal vortex tubes and turn into the directions depicted by the broken arrows in the figures, hence always increasing the angle between the vorticity vectors and the streamwise direction compared to that of the centerline of the longitudinal vortex tubes. Our DNS results show that the solid particles do change the magnitude of this term $(-S\partial u_i/\partial x_2)$, and thus modify vorticity dynamics. Figure 19 shows the pdf of $(-S\partial u_i/\partial x_2)$ for cases A–C at $T=3$. The figure indicates an increase in the magnitude of $(-S\partial u_i/\partial x_2)$ for cases B and C as compared to that of case A. This is seen in the increase of the amplitude of the pdf of cases B and C at large values of $|-S\partial u_i/\partial x_2|$ and a decrease in the amplitude of the pdf around $-S\partial u_i/\partial x_2=0$. Thus, the vorticity vectors of case B deviate more from the axis of their longitudinal vortex tubes than those of case C. Figure 20 shows the pdf$(-S\partial u_i/\partial x_2)$ for cases A, D, and E at $T=6$. It is seen that the tails of the pdf$(-S\partial u_i/\partial x_2)$ for cases D and E have larger amplitudes than those of case A, signifying an increase in the value of $-S\partial u_i/\partial x_2$ for cases D and E as compared to case A. Also, it is clear that the value of $-S\partial u_i/\partial x_2$ for case D is larger than that of case E, causing a larger deviation between the vorticity vectors and the axis of their longitudinal vortex tubes of case D than those of case E. It should be noted that the larger the deviation of the vorticity vector from the longitudinal vortex tube axis, the smaller the magnitude of the vorticity component along the vortex tube axis.

3. Modification of the orientation of vorticity vectors

Further evidence of the changes in the directions of the vorticity vectors due to the particles, discussed above, is manifested in the changes of the angles ϕ and ψ, between the vorticity vector and the horizontal and spanwise directions respectively (Fig. 21). These angles are calculated from the three vorticity components

$$\omega_1=|\omega|\cos\phi\sin\psi, \quad \omega_2=-|\omega|\cos\phi\cos\psi,$$
$$\omega_3=|\omega|\sin\phi. \tag{28}$$

Figure 22 shows the pdf(ϕ) for cases A–C at $T=4$. It is seen that the amplitude of the pdf of case B, compared to that

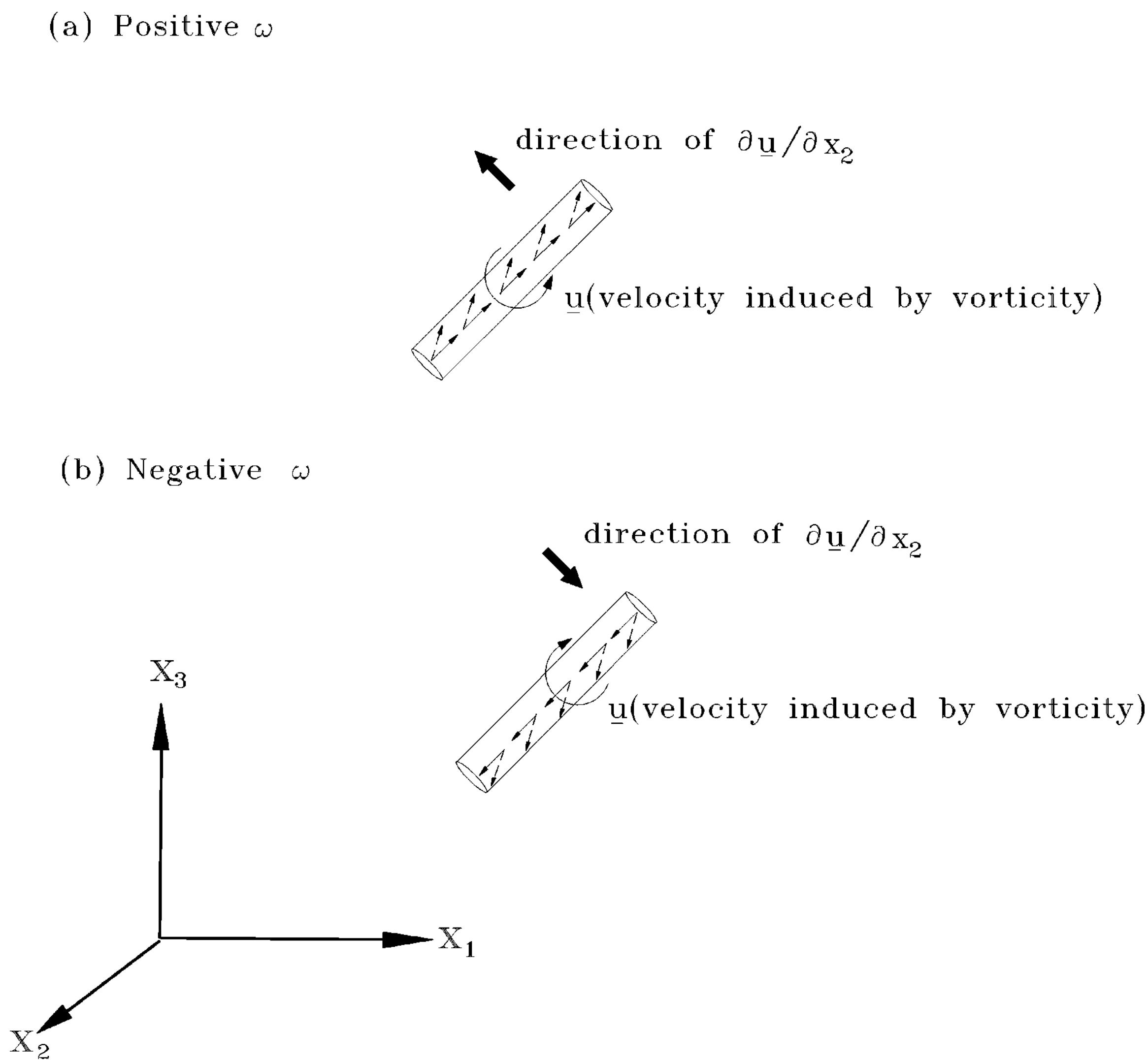

FIG. 18. Deviation in orientation between a longitudinal vortex tube and vorticity therein.

of case A, increases mainly around large values of $|\phi|$ and slightly around $\phi=0$, signifying an increase in the probability of having large values of ϕ ($45° < |\phi| < 90°$) in case B as compared to case A. On the other hand, the pdf(ϕ) of case C is nearly the same as that of case A, except to a slight increase around $\phi=0$. Thus, on the average the vorticity vectors of case C will be more aligned with the streamwise direction as compared to case A, while those of case B deviate more from the streamwise direction. The increase of ϕ in case B is due the increase in the magnitude of $(-S\partial u_i/\partial x_2)$ discussed in the previous subsection. The increase in the pdf around $\phi=0$, in cases B and C as compared to case A, is due to the increase in the term $S\omega_3$ [the first term in the second bracket of Eq. (26)]. This term converts the vertical vorticity into the streamwise direction and is shown by Kida and Tanaka[18] to cause the vorticity vector to move towards the streamwise direction. Since $S=1$ in our flow, the term $S\omega_3$ equals ω_3. Our results show that ω_3 of cases B and C is larger than that of case A.

Figure 23 shows the pdf(ϕ) of cases A, D, and E at $T=4$. The figure shows that the increase in the angle ϕ of case D as compared to case A is in the range $45° < |\phi| < 90°$,

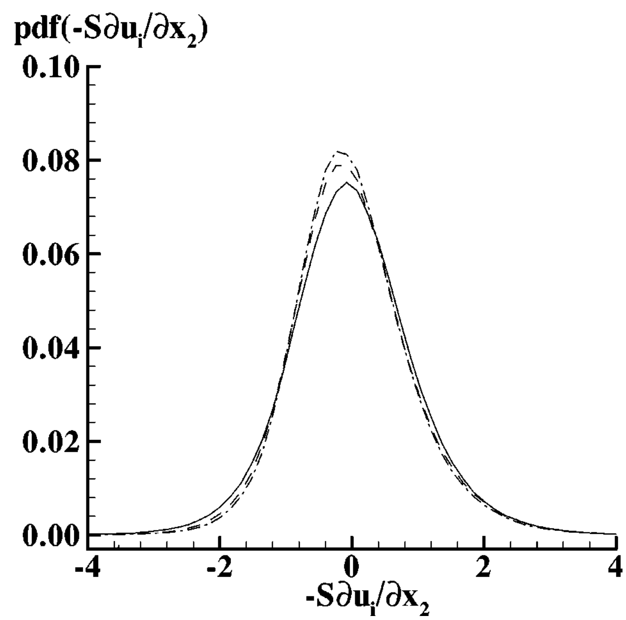

FIG. 19. pdf($-S\partial u_i/\partial x_2$) at $T=3$. Case B (solid line), case C (dashed line), case A (dash–dot line).

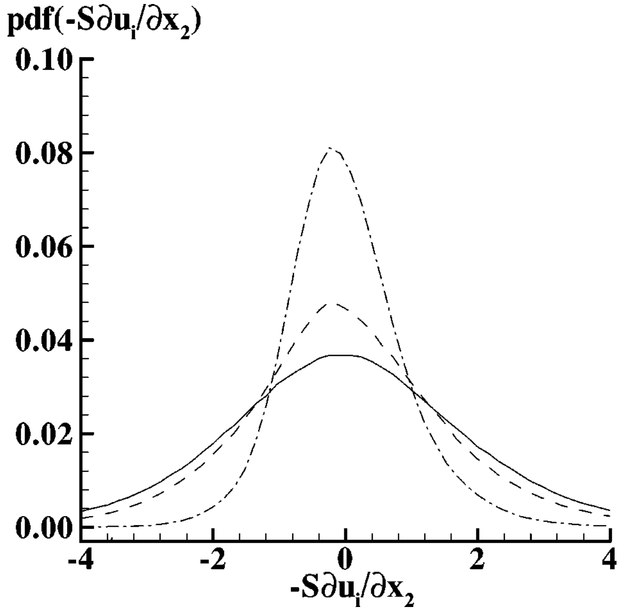

FIG. 20. pdf$(-S\partial u_i/\partial x_2)$ at $T=6$. Case D (solid line), case E (dashed line), case A (dash–dot line).

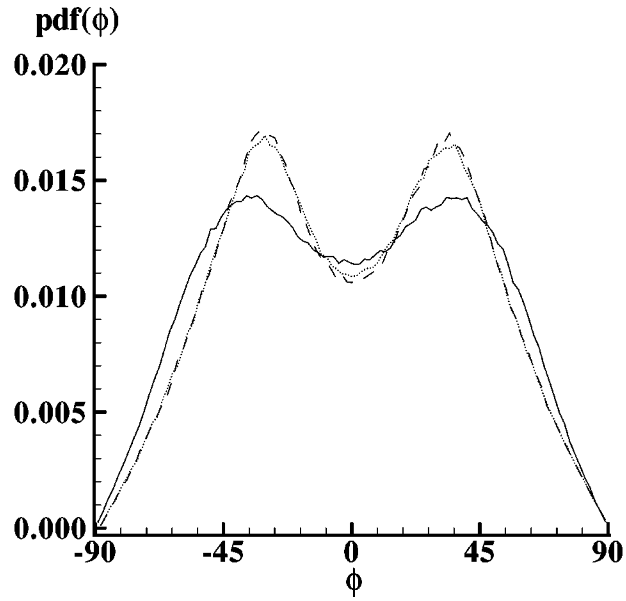

FIG. 22. pdf of vorticity angle ϕ at $T=4$. Case B (solid line), case C (dotted line), case A (dashed line).

while that of case E is for smaller values of ϕ. The behavior of the angle ϕ of cases D and E relative to that of case A can be explained partially by the increase in $(-S\partial u_i/\partial x_2)$ in cases D and E as discussed in the previous subsection. However, the effect of the particles source term (due to the gravity) on vorticity is dominant. Figures 24–26, show the source terms $b_i, i=1,2,3$, respectively, at $T=4$ for cases D and E. Comparing the pdf of b_i of cases D and E with those of ω_i of the two cases seen in Figs. 38–40, we see a direct proportionality. For case E, ω_1 increases (Fig. 38) due to b_1 (Fig. 24), and the increase in ω_3 for case D (Fig. 40) is due to b_3 (Fig. 26). The increase in ω_1 due to the increase of b_1 in case E leads to the inclination of the vorticity vector towards the streamwise direction, thus increasing pdf(ϕ) of case E around $\phi=0$ (Fig. 23).

Now, we consider the pdf of the angle ψ (the angle between the vorticity vector and x_2 direction, Fig. 21). Figure 27 shows the pdf(ψ) for cases A–C at $T=4$. It is seen that the pdf(ψ) of case C is nearly identical to that of case A, whereas the pdf(ψ) of case B increases around $\psi=0$ and $\psi=\pm 180°$ as compared to case A. Figure 28 shows the pdf(ψ) for cases A, D, and E at $T=4$. It is seen that the vorticity vectors in case D (gravity in $-x_1$ direction) tend to be aligned in the spanwise direction, as indicated by the larger magnitude of the pdf around $\psi=0$ and $\psi=\pm 180°$. Also, the vorticity vectors in case E (gravity in $-x_3$ direction) tend to be aligned with the spanwise direction but to a lesser extent than in case D as indicated by larger amplitudes

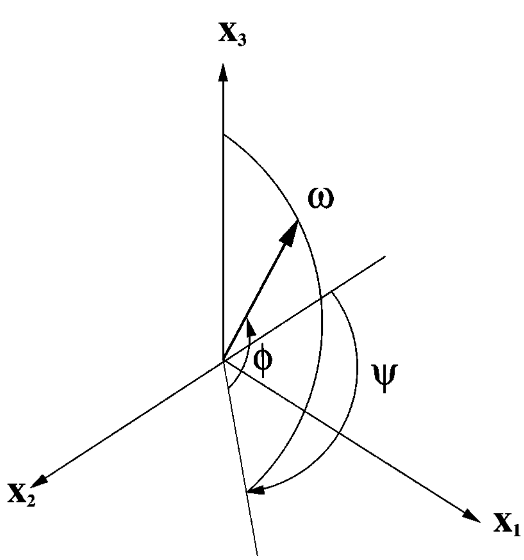

FIG. 21. Vorticity vector angles ϕ and ψ.

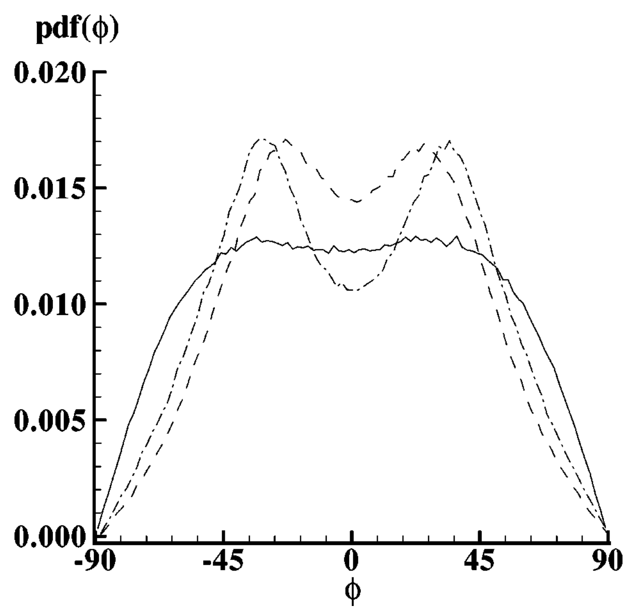

FIG. 23. pdf of vorticity angle ϕ at $T=4$. Case D (solid line), case E (dashed line), case A (dash-dot line).

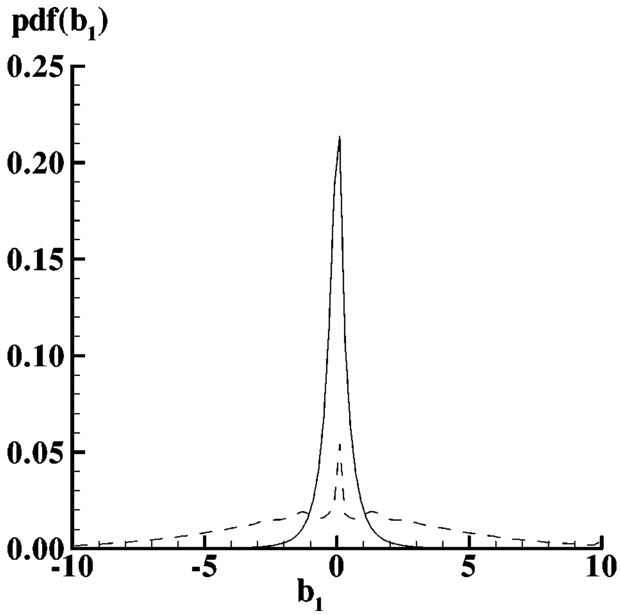

FIG. 24. pdf of the particles source term in ω_1 equation at $T=4$. Case D (solid line), case E (dashed line).

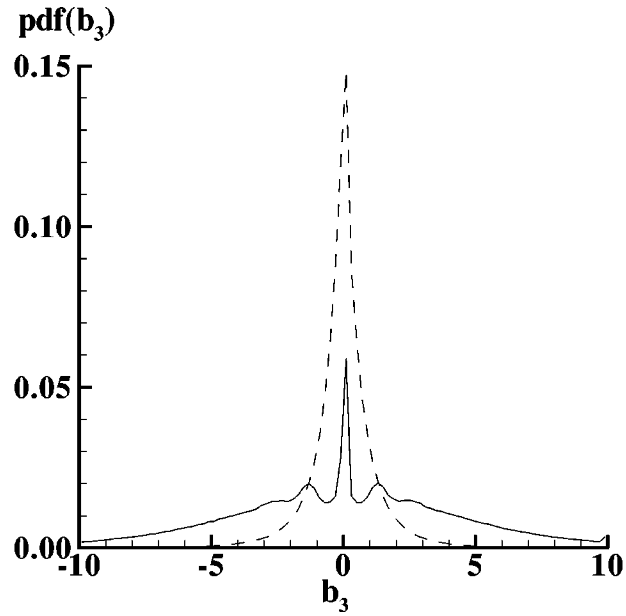

FIG. 26. pdf of the particles source term in ω_3 equation at $T=4$. Case D (solid line), case E (dashed line).

of the pdf(ψ), as compared to case A, around $\psi \approx \pm 135°$ instead of $\psi = \pm 180°$ seen in case D. The increase in pdf(ψ) at $\psi=0$ is smaller in case E compared to case D.

In order to explain the reasons for the behavior of the angle ψ, we consider the transport equation of the spanwise vorticity ω_2, written in the $x_s - x_n$ coordinates of the longitudinal vortex tube (see Fig. 29)

$$\frac{D\omega_2}{Dt} = \omega_s \frac{\partial u_2}{\partial x_s} + \omega_n \frac{\partial u_2}{\partial x_n} + (\omega_2 - S)\frac{\partial u_2}{\partial x_2} + \upsilon \nabla^2 \omega_2 + b_2 . \tag{29}$$

The first two terms on the RHS of (29) represent vorticity conversion from the ω_s and ω_n components to ω_2 by velocity fluctuations. The third term represents a contribution from the spanwise stretching of both the mean vorticity $(-S)$ and ω_2. The fourth term is vorticity diffusion, while the last term is the particles source term in the $x_s - x_n$ coordinates.

Figures 29(a) and 29(b) show two longitudinal vortex tubes with the vorticity vectors deviating from their longitudinal vortex tube axis, as explained earlier in Fig. 18, for (a) positive vorticity and (b) negative vorticity. The velocity induced by the vortices is represented by the curved arrows around the longitudinal vortex tubes. Figures 29(a) and 29(b) show that the term $\omega_n \partial u_2 / \partial x_n$ always has a positive contri-

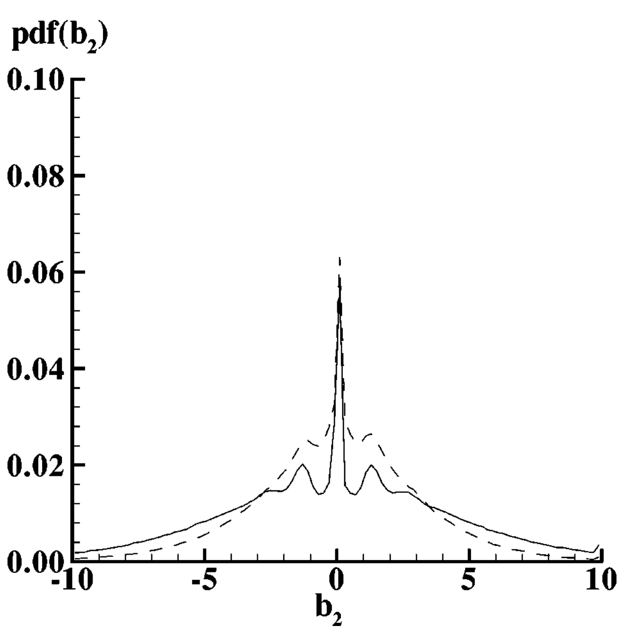

FIG. 25. pdf of the particles source term in ω_2 equation at $T=4$. Case D (solid line), case E (dashed line).

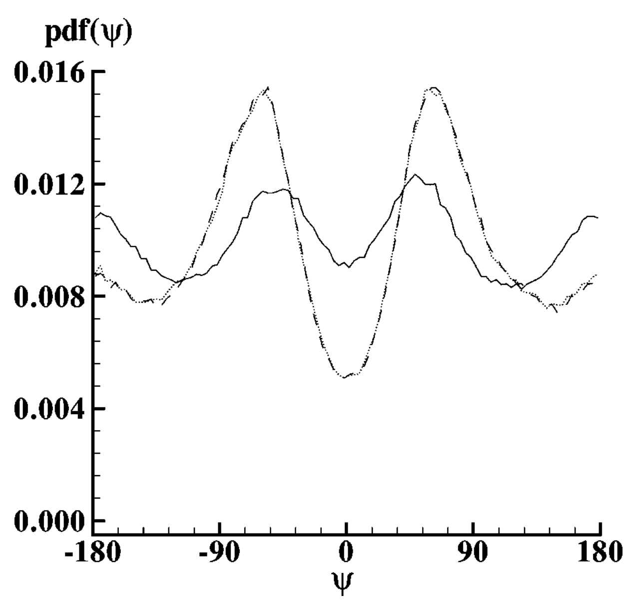

FIG. 27. pdf of vorticity angle ψ at $T=4$. Case B (solid line), case C (dotted line), case A (dashed line).

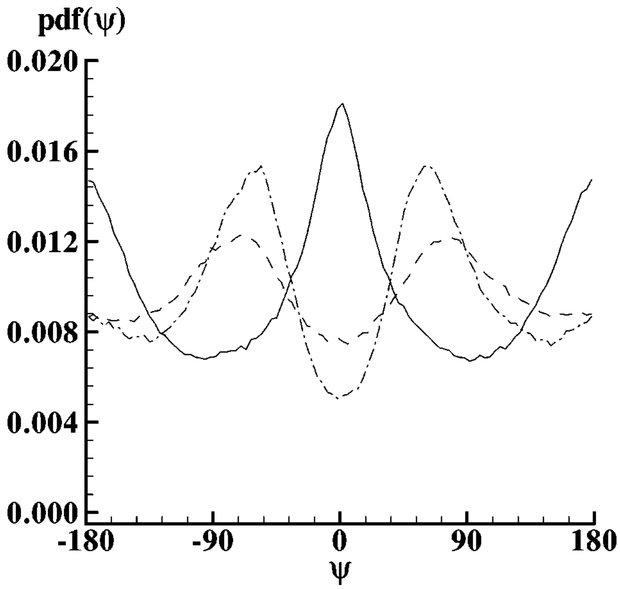

FIG. 28. pdf of vorticity angle ψ at $T=4$. Case D (solid line), case E (dashed line), case A (dash–dot line).

bution to ω_2 for both positive and negative vortices [e.g., in Fig. 29(a), ω_n is positive and the derivative of u_2 of the induced velocity, $\partial u_2/\partial x_n$, is also positive; both quantities are negative in Fig. 29(b)]. Our results show that the pdf($\omega_n \partial u_2/\partial x_n$) for case C at $T=4$ is nearly identical to that of case A (figure is not shown), in agreement with the behavior of the angle ψ, seen in Fig. 27 for the two cases. In case B, the tail of the pdf($\omega_n \partial u_2/\partial x_n$) has larger amplitude than that of case A (figure is not shown), indicating an increase in the value of $\omega_n \partial u_2/\partial x_n$ of case B as compared to case A. The increase in $\omega_n \partial u_2/\partial x_n$ contributes to the increase of positive ω_2. The particles source term b_2 also increases ω_2. Our results show that b_i of case B are larger than those of case C (figures are not shown). The effect of this source term is to increase the vorticity component in each of the three directions.

Kida and Tanaka[18] showed that the third term in (29) represents a transformation of the mean vorticity into fluctuating negative ω_2, i.e., in the direction of the mean vorticity $-S$. Our results (figure is not shown) indicate that the

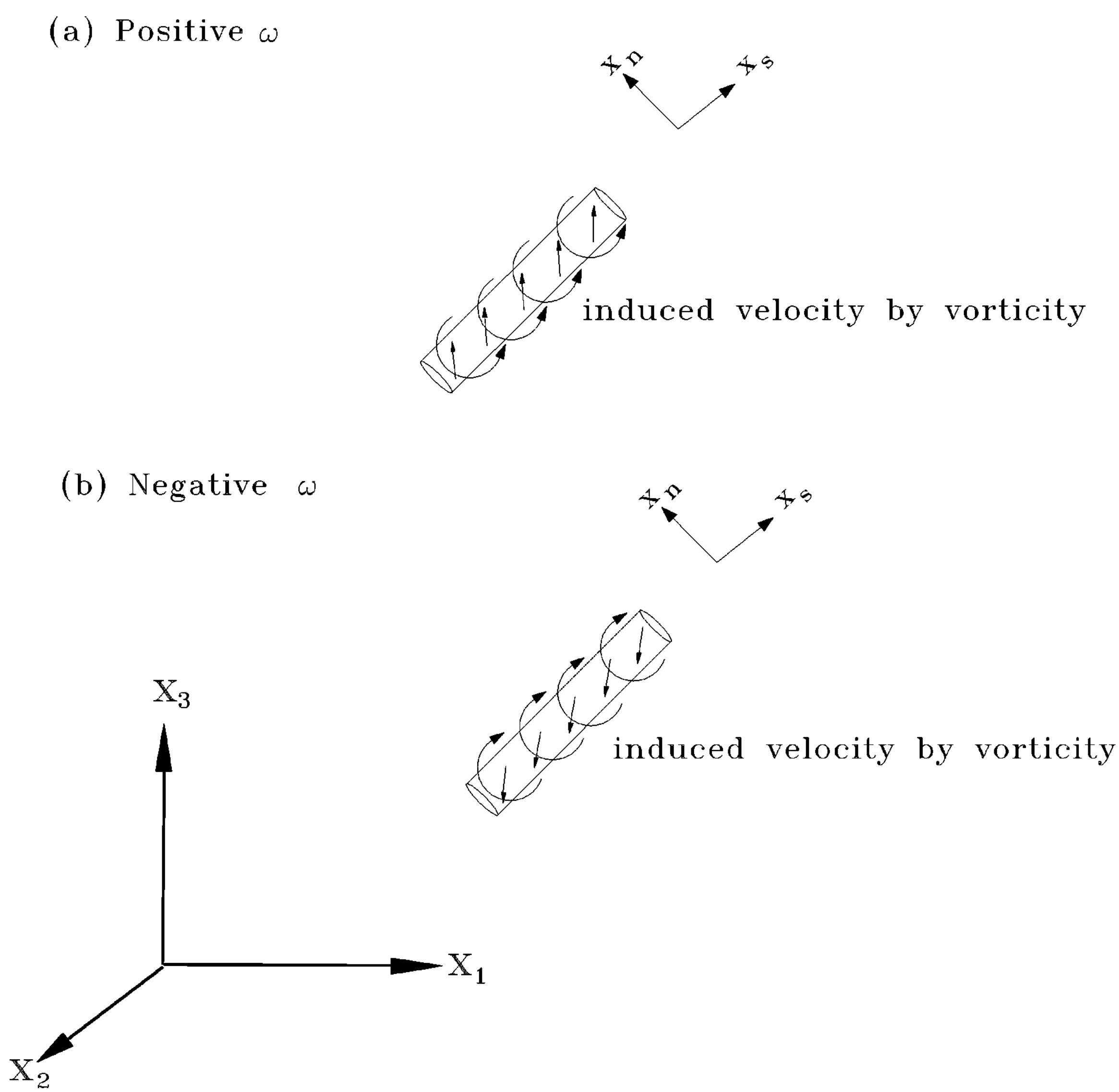

FIG. 29. The turning of vorticity vectors towards x_2 axis.

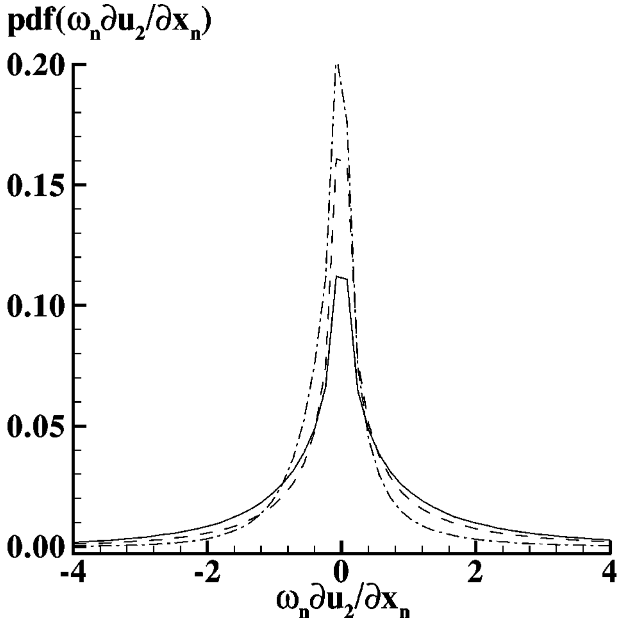

FIG. 30. pdf($\omega_n \partial u_2/\partial x_n$) at $T=6$. Case D (solid line), case E (dashed line), case A (dash–dot line).

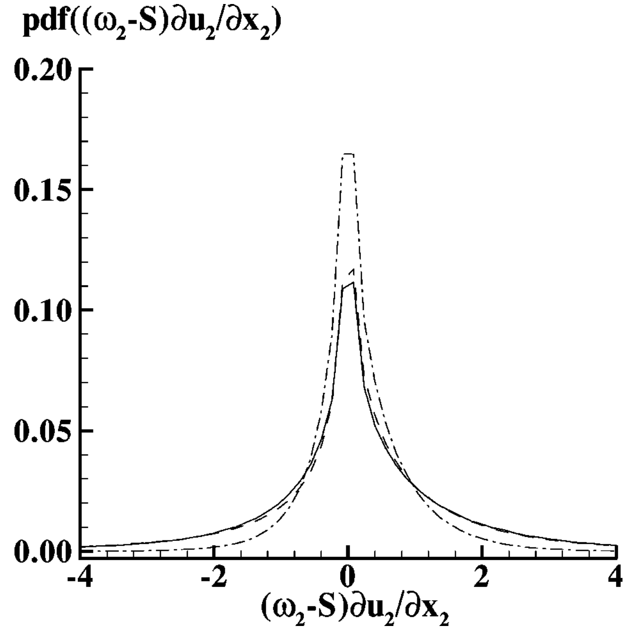

FIG. 31. pdf($(\omega_2 - S)\partial u_2/\partial x_2$) at $T=6$. Case D (solid line), case E (dashed line), case A (dash–dot line).

pdf($(\omega_2 - S)\partial u_2/\partial x_2$) of case C is nearly identical to that of case A, i.e., consistent with pdf(ψ), Fig. 27. In case B, the magnitude of pdf($(\omega_2 - S)\partial u_2/\partial x_2$) at $T=4$ is less that that of case A (figure is not shown). Thus, the main reason for the increase of ω_2 in case B is the particle source term b_2. The increase of ω_2 causes the vorticity vector to move towards the x_2 axis, and hence the increase in the the probability of ψ near $\psi=0,\pm 180°$.

As discussed earlier, the term $\omega_n \partial u_2/\partial x_n$ always has a positive contribution to ω_2, while $(\omega_2 - S)\partial u_2/\partial x_2$ has a negative contribution on average as shown by Kida and Tanaka.[18] Thus, the increase of either of these two terms will lead to the inclination of the vorticity vector in either the positive or negative spanwise direction, respectively. Figure 30 shows the pdf($\omega_n \partial u_2/\partial x_n$) for cases A, D, and E at $T=6$. The figure shows that the magnitude of the pdf of cases D and E is larger at the tails than that of case A, signifying an increase in the value of $\omega_n \partial u_2/\partial x_n$ for cases D and E over that of case A. The pdf($(\omega_2 - S)\partial u_2/\partial x_2$) for the same cases at $T=6$ is shown in Fig. 31. It is seen that the amplitude of the pdf tails for cases D and E has larger values than that of case A, reflecting an increase in the value of $(\omega_2 - S)\partial u_2/\partial x_2$ for cases D and E compared to case A. The increase in the values of $\omega_n \partial u_2/\partial x_n$ and $(\omega_2 - S)\partial u_2/\partial x_2$ for cases D and E over that of case A leads to an increase in the inclination of the vorticity vectors towards the positive and negative spanwise directions for cases D and E as compared to case A. In addition, the increase in the magnitude of the particles source term b_2 shown in Fig. 25 increases the magnitude of ω_2 and hence increases the alignment of vorticity vector with the spanwise direction.

In order to visualize the changes in vorticity field due to the particles, we extracted the topology of the centerlines of the tubular vortices from our DNS results for all the cases at $T=6$. Figures 32(a) and 32(b) show the extracted tubular vortices for cases A and B, respectively. The figures show the lines connecting the loci of the vortex cores identified by the local minimum pressure as outlined by Miura and Kida.[19] The color intensity denotes the sum of the two positive eigenvalues of the pressure Hessian $[\partial^2/\partial x_i x_j(p)]$ and represents the strength of vortices. It is clear that the angle between the horizontal plane and the centerlines of the vortices in case B, Fig. 32(b), is larger than that of case A, Fig. 32(a). On the other hand the inclination of the tubular vortices in case C (figure is not shown) is nearly the same as in case A, consistent with the behavior of the vorticity angles in this case. Our results of the extracted tubular vortices for cases D and E (figures are not shown) show that the tubular vortices of case D are more aligned with the vertical and spanwise directions than in case A, while in case E the tubular vortices are more inclined towards the spanwise direction and to some extent toward the streamwise direction, consistent with the behavior of the angles ϕ and ψ discussed earlier.

The effects of the particles on the orientation angles (ϕ and ψ) of the vorticity vectors are reflected in the changes of the magnitudes of vorticity components, ω_i. Figures 33–35, show the pdf of $\omega_i, i=1,2,3$ for cases A–C at $T=4$. It is seen that in case C, the three components of vorticity are increased as compared to case A with the largest increase occurring in ω_1, consistent with the increase in the pdf(ϕ) near $\phi=0$ (i.e., vorticity vector is more aligned with x_1) seen in Fig. 22. On the other hand, in case B, the vorticity vector is more inclined towards the vertical and spanwise directions and away from the streamwise direction consistent with the increase in ω_2 and ω_3 and the reduction of ω_1. The changes in $\omega_i, i=1,2,3$ of cases B and C are reflected in the changes in ω_s and ω_n as shown in Figs. 36 and 37. It is seen that with the increase in the magnitude of the pdf(ϕ) for $\phi=0$ in case C, the vorticity vectors become more aligned with the axes of their vortex tubes resulting in larger ω_s and

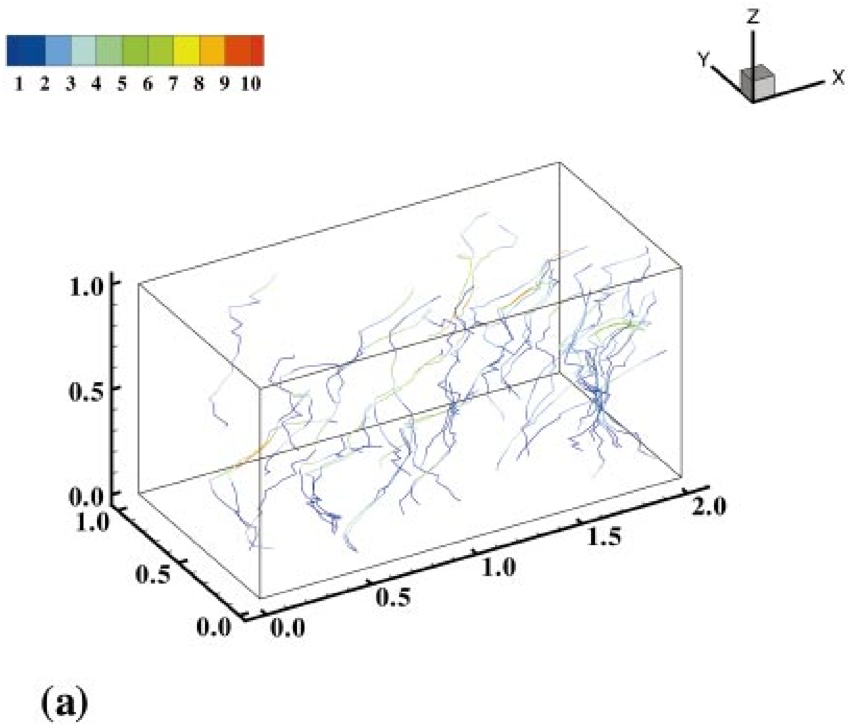

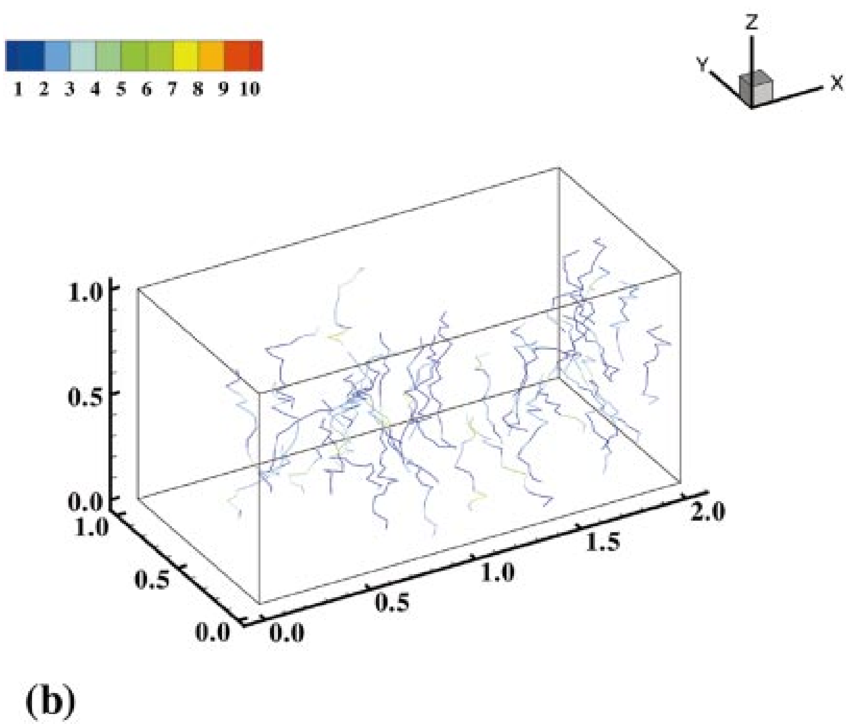

FIG. 32. (Color) Extracted tubular vortices at $T=6$. (a) Case A, (b) case B.

smaller ω_n than in case A. On the other hand, in case B, the increase in the pdf(ϕ) for large values of ϕ, is associated with larger deviation between the vorticity vectors and their longitudinal vortex tubes. This increase in deviation results in a smaller ω_s (36) and larger ω_n (37) for this case. Figures 38–40 show the distribution of ω_i, $i=1,2,3$ for cases A, D, and E at $T=4$. It is seen that in case D, where the vorticity vector is inclined towards the x_2 and x_3 directions, the vorticity components ω_2 and ω_3 increased substantially, while ω_1 increased only slightly as compared to case A. Similarly, the vorticity increase in case E is mainly in ω_1 and ω_2, while ω_3 increased the least, is consistent with the changes in ϕ and ψ. The same results are reflected in the relative distribution of ω_s and ω_n. Figures 41 and 42 show the pdf of ω_s and ω_n for cases A, D, and E at $T=4$. The figures show that due to the increase in vorticity strength and the relatively

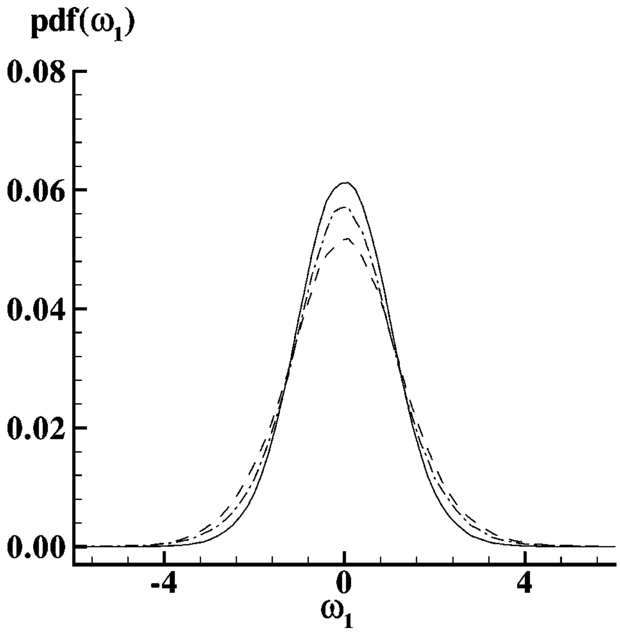

FIG. 33. pdf of vorticity component ω_1 at $T=4$. Case B (solid line), case C (dashed line), case A (dash–dot line).

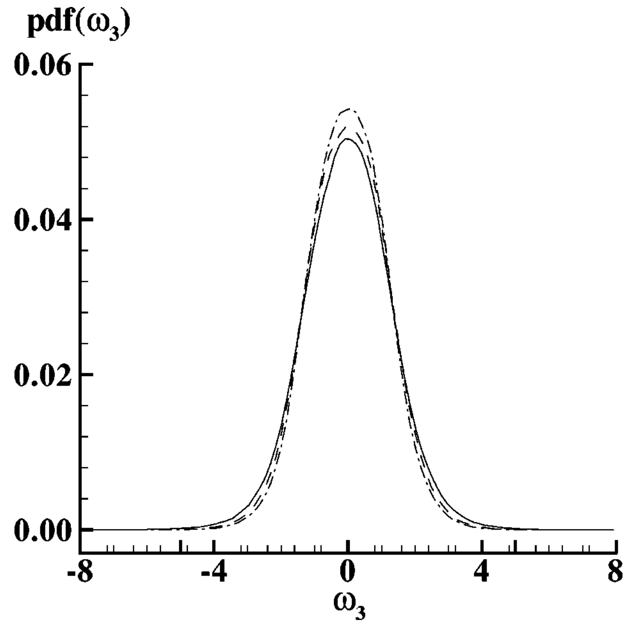

FIG. 35. pdf of vorticity component ω_3 at $T=4$. Case B (solid line), case C (dashed line), case A (dash–dot line).

small changes in the angle ϕ in case E, both ω_s and ω_n are increased relative to case A. On the other hand, the large increase in the magnitude of pdf(ϕ) for large values of ϕ in case D is consistent with the deviation of the vorticity vectors more from their longitudinal vortex tube axis than in case A, and a smaller increase in ω_s than in ω_n.

4. Modification of the production rate of turbulence energy

The decrease or increase in ω_s leads respectively, to a reduction or augmentation in the turbulence energy production rate, $S\langle u_1 u_3 \rangle$. Kida and Tanaka[10] showed that the regions of high turbulence energy production are concentrated between counter-rotating ω_s vortices. Figures 43(a) and 43(b) show contours of typically high Reynolds stress, $u_1 u_3 = -0.002$, denoted by black closed contours superimposed on contours of ω_s in an $x_2 - x_n$ plane at $T=4$ for cases A and B. The figures show that regions of large turbulence production rate are sandwiched between pairs of counter rotating ω_s vortices. Note that regions where Reynolds stress magnitude 0.002 are enclosed within the black contours. Also, it is clear that the magnitude of ω_s is reduced in case B compared to case A, as indicated by lower color intensity

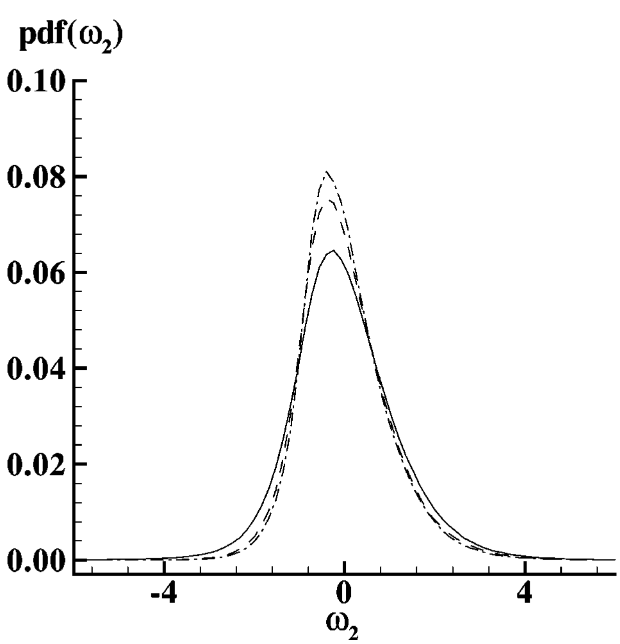

FIG. 34. pdf of vorticity component ω_2 at $T=4$. Case B (solid line), case C (dashed line), case A (dash–dot line).

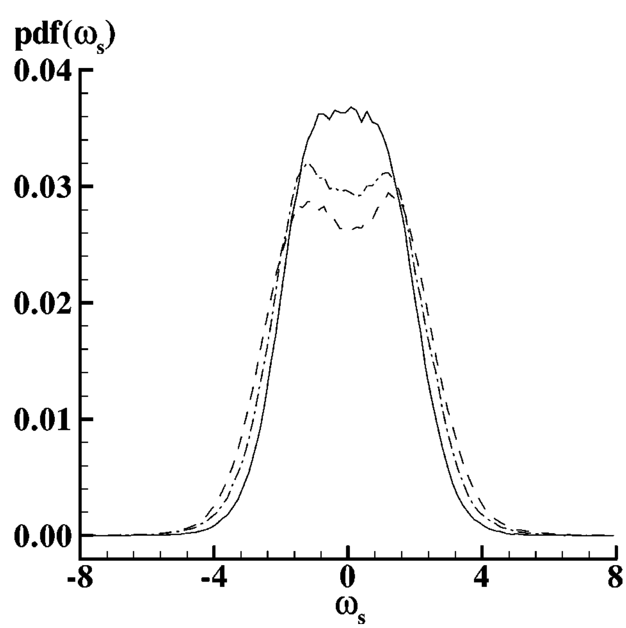

FIG. 36. pdf of vorticity component along the longitudinal vortex tube ω_s at $T=4$. Case B (solid line), case C (dashed line), case A (dash–dot line).

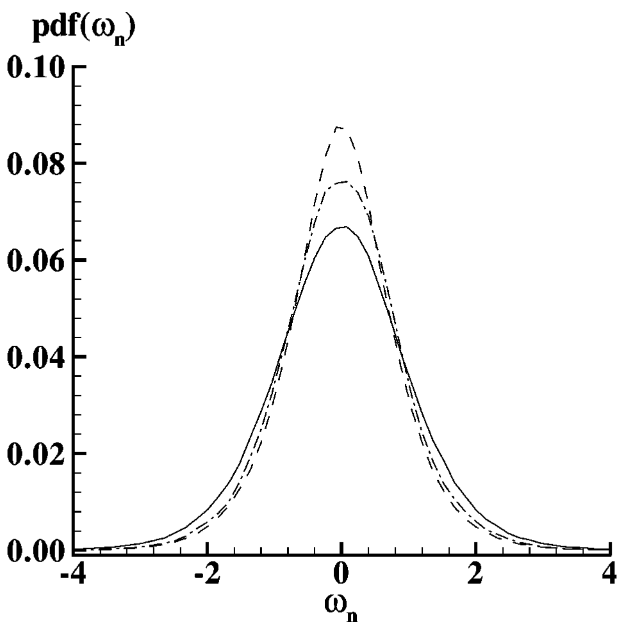

FIG. 37. pdf of vorticity component normal to the longitudinal vortex tube ω_n at $T=4$. Case B (solid line), case C (dashed line), case A (dash–dot line).

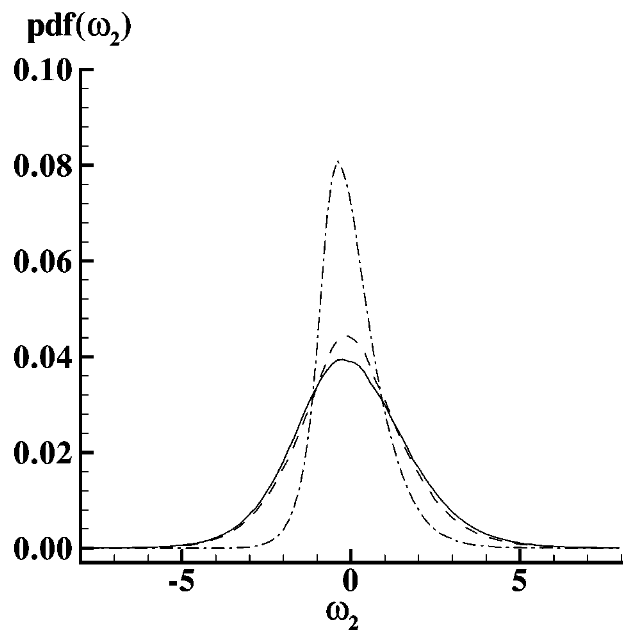

FIG. 39. pdf of vorticity component ω_2 at $T=4$. Case D (solid line), case E (dashed line), case A (dash–dot line).

(blue and red) in Fig. 43(b) as compared to Fig. 43(a). Furthermore, black closed contours of large turbulence production rate regions occupy smaller area in Fig. 43(b) as compared to Fig. 43(a), signifying a reduction in turbulence energy production in case B. In case C (figure is note shown) the changes are smaller, consistent with the small increase in the production rate in this case. Similar results are obtained for cases D and E (figures are not shown), where larger zones of turbulence production rate are sandwiched between counter-rotating ω_s vortices, than those of case A.

In order to further examine the relation between turbulence energy production rate and the vorticity, we derive an equation for $\langle u_1 u_3 \rangle$ based on Lele's[20] equation for the Reynolds stresses and vorticity [Eq. (6) in his paper]. Here, we rewrite this equation after dropping the diffusion, dissipation, advection, pressure strain, and source terms. It should be noted that, since we are only interested in a relation between the production rate of $\langle u_1 u_3 \rangle$ and vorticity components, we kept only the terms that have $\mathbf{u} \times \boldsymbol{\omega}$. The resulting equation for $\langle u_1 u_3 \rangle$ takes the form

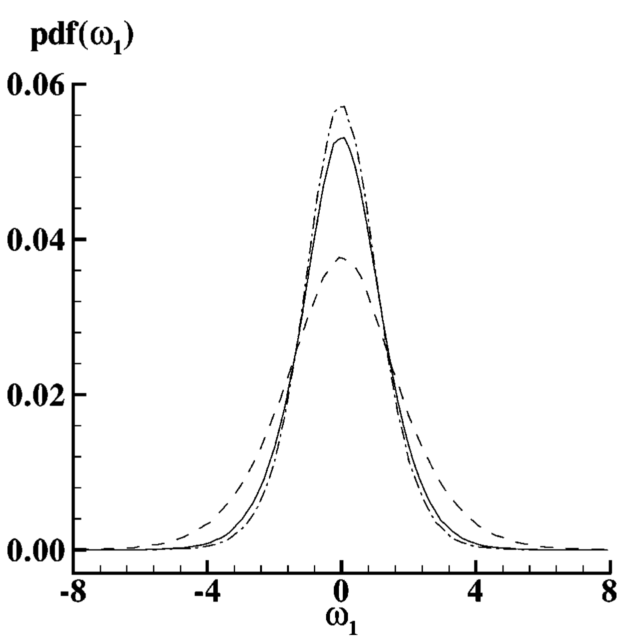

FIG. 38. pdf of vorticity component ω_1 at $T=4$. Case D (solid line), case E (dashed line), case A (dash–dot line).

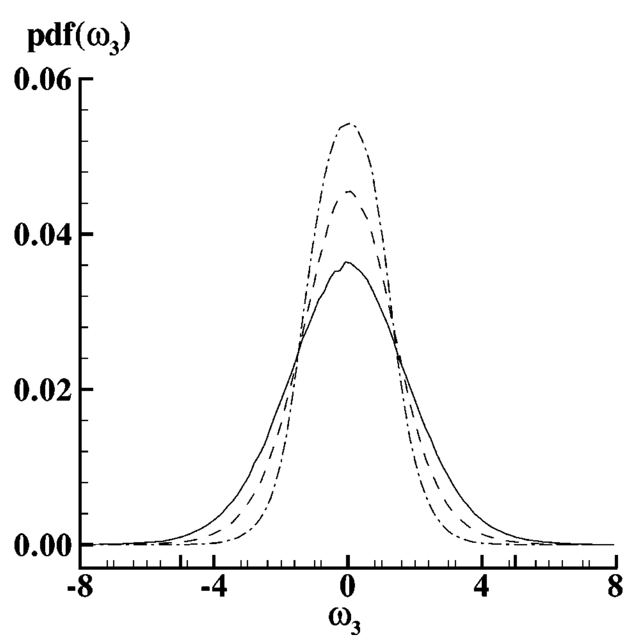

FIG. 40. pdf of vorticity component ω_3 at $T=4$. Case D (solid line), case E (dashed line), case A (dash–dot line).

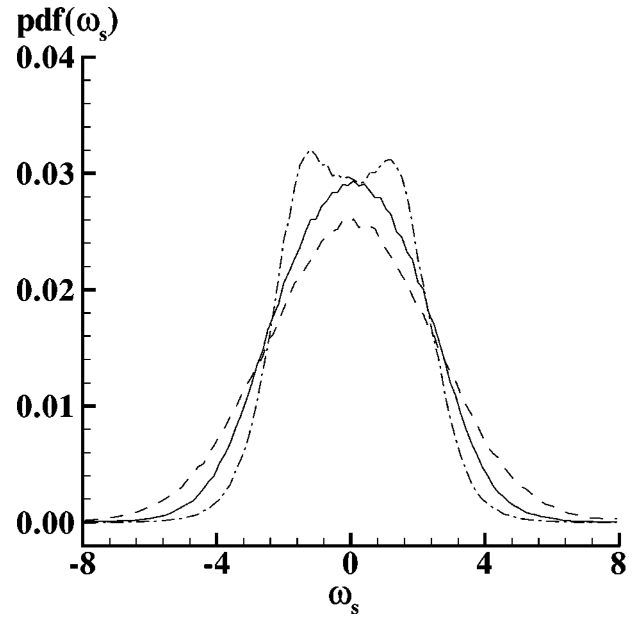

FIG. 41. pdf of vorticity component along the longitudinal vortex tube ω_s at $T=4$. Case D (solid lines), case E (dashed lines), case A (dash–dot lines).

$$\frac{\partial\langle u_1u_3\rangle}{\partial t}\approx\langle u_1(\mathbf{u}\times\boldsymbol{\omega})_3\rangle+\langle u_3(\mathbf{u}\times\boldsymbol{\omega})_1\rangle, \tag{30}$$

which can be expanded in the form

$$\frac{\partial\langle u_1u_3\rangle}{\partial t}\approx\langle u_1u_3\omega_3\rangle-\langle u_3u_3\omega_2\rangle+\langle u_1u_1\omega_3\rangle -\langle u_1u_2\omega_1\rangle. \tag{31}$$

Let ζ be the angle between the longitudinal vortex tube and the x_1 axis. We then obtain the following relations between ω_1, ω_3, ω_s and ω_n:

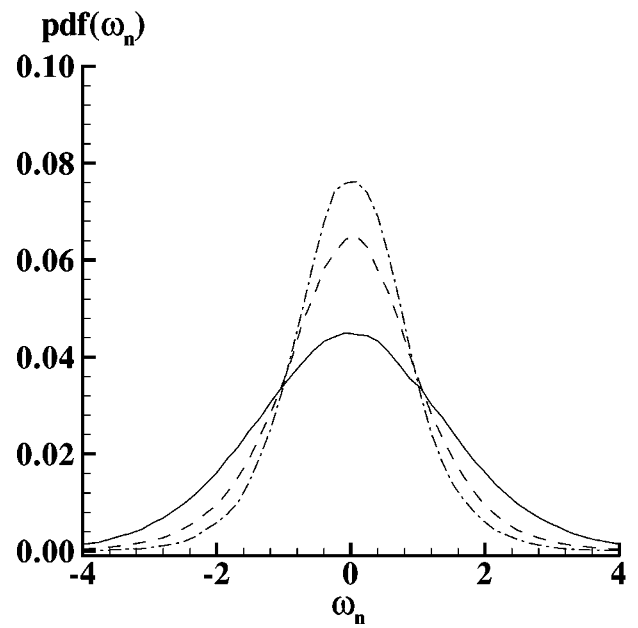

FIG. 42. pdf of vorticity component normal to the longitudinal vortex tube ω_n at $T=4$. Case D (solid lines), case E (dashed lines), case A (dash–dot lines).

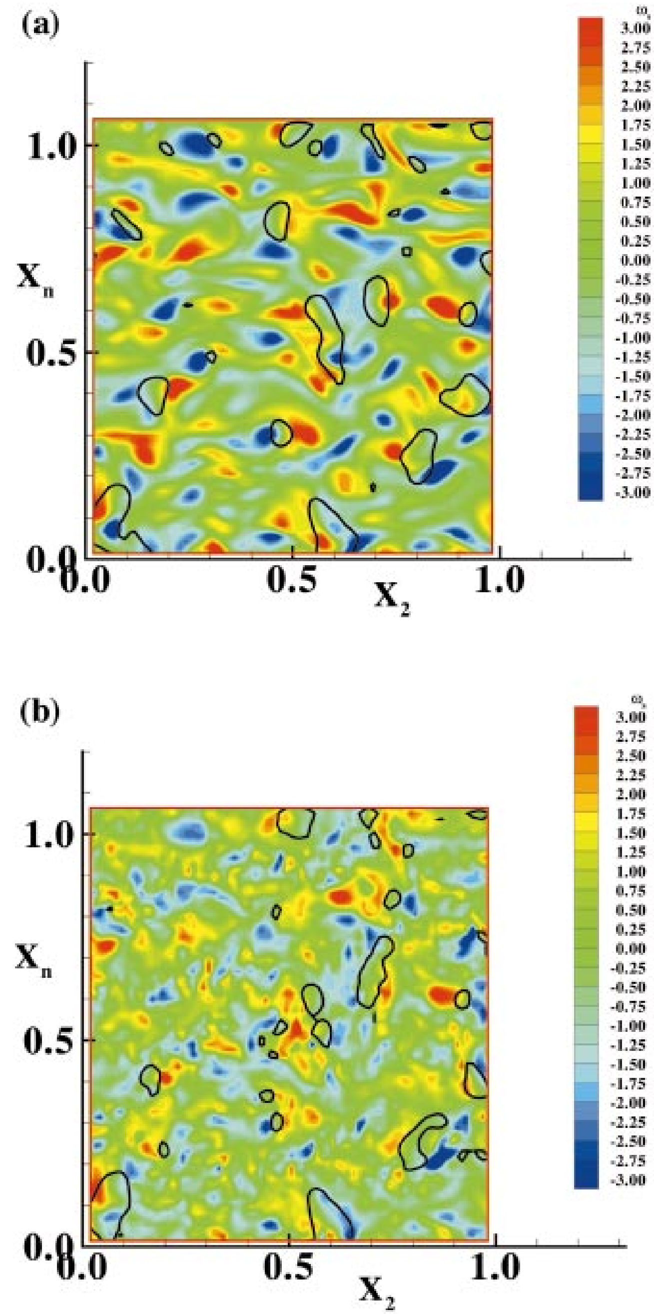

FIG. 43. (Color) Contours of $u_1u_3=-0.002$ (closed black contours) superimposed on ω_s at $T=4$. (a) Case A, (b) case B.

$$\omega_1=\omega_s\cos\zeta-\omega_n\sin\zeta, \tag{32}$$

$$\omega_3=\omega_s\sin\zeta+\omega_n\cos\zeta. \tag{33}$$

Substitution of (33) in Eq. (31), we get

$$\frac{\partial\langle u_1u_3\rangle}{\partial t}\approx\langle((u_1u_3+u_1^2)\sin\zeta-u_1u_2\cos\zeta)\omega_s\rangle +\langle((u_1u_3+u_1^2)\cos\zeta-u_1u_2\sin\zeta)\omega_n\rangle +\langle u_1u_3\omega_2\rangle. \tag{34}$$

The three terms on the RHS of Eq. (34) represent the contribution of ω_s, ω_n, and ω_2 to the production rate of $\langle u_1u_3\rangle$, respectively. Time development of these three terms are

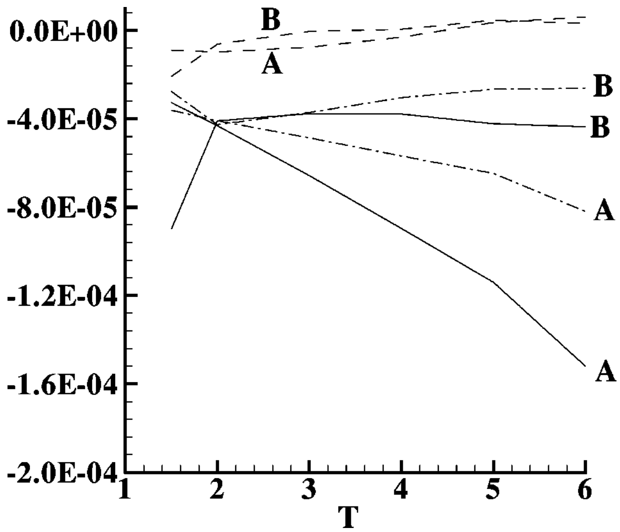

FIG. 44. Time development of the terms contributing to Reynolds stress production. ω_s term (solid line), ω_n term (dashed line), ω_2 term (dash–dot line).

shown in Fig. 44 for cases A and B. It is clear that the ω_s term has the dominant contribution to the production rate of $\langle u_1 u_3 \rangle$ in both cases, and its magnitude is reduced due to the coupling between the solid particles and fluid (case B), which is consistent with the reduction of turbulence production rate in case B. Similar results are obtained for the other cases and hence are not shown here.

The results and discussion presented above in Secs. III C 1–III C 4 show that solid particles injected in a homogeneous turbulent shear flow modulate the turbulence structure by modifying the dynamics of vorticity. The main mechanisms responsible for this modification can be summarized as follows. The particles, due to their drag, create local velocity gradients in the surrounding fluid, leading to an increase in the magnitude of the local strain rate, which results in an increase in the dissipation rate of turbulence kinetic energy. Furthermore, particles whose $\tau_p \approx \tau_K$ tend to accumulate in regions of low vorticity, resulting in a further increase of the local velocity gradients of the surrounding fluid, which in turn modifies the vorticity dynamics. The augmented velocity gradients change the alignment of the vorticity vectors with their longitudinal vortex tubes. If the alignment between the vorticity vector and its longitudinal vortex tube increases, so does the magnitude of the vorticity component along the axis of the vorticity tube, ω_s, and vice versa. Since regions of high turbulence production rate are sandwiched between counter-rotating ω_s vortices. An increase in ω_s augments the rate of turbulence production, and vice versa.

D. Effect of varying the mass loading, particle inertia, and drift velocity on turbulence modulation

It was mentioned earlier that for a clear presentation of the physical mechanisms responsible for modifying the turbulence structure we selected only four out of the ten simulations we performed. In this section, we examine the results of all the ten simulations to perform a parametric study of the effects of varying mass loading, particle inertia and drift velocity on turbulence modulation. The parameters of the six additional cases are presented in Table III below.

In order to vary mass loading, we consider case B, where the particle time constant is unity, and vary the number of particles in the computational domain. Changing the number of particles while keeping the particle inertia constant, changes the mass loading. In order to vary particle inertia, we keep the particle diameter constant and vary the particle material density. On the other hand, fixing the mass loading while varying the particle inertia, changes the number of particles. The heavier the particle is, the smaller the number of particles used. In the following we discuss only the modifications of the turbulence kinetic energy, $E(T)$, and its rate of dissipation, $\epsilon(T)$.

Figure 45 shows the effect of varying the particle inertia on the temporal development of turbulence kinetic energy $E(T)$, and its rate of dissipation, $\epsilon(T)$. We consider four particles whose response times are: $\tau_p = 0.1, 0.25, 0.5$, and 1.0. It is seen that the smallest particles ($\tau_p = 0.1$) increase the turbulence kinetic energy, while heavier particles ($\tau_p > 0.1$) reduce it. Druzhinin and Elghobashi[25] obtained similar results for micro-particles ($\tau_p \ll \tau_K$) in decaying isotropic turbulence where the micro-particles reduced the decay rate of turbulence energy. Druzhinin and Elghobashi used the two-fluid approach in their simulations and provided an explanation of this phenomenon based on asymptotic solution. As the particle inertia increases, the rate of reduction of turbulence kinetic energy is increased, with the largest increase observed for $\tau_p = 1.0$. The figure also shows that, as expected, the modification of the rate of turbulence energy dissipation, $\epsilon(T)$, is proportional to that of $E(T)$. The turbulence energy dissipation rate for all the two-way coupling cases starts larger than that of the particles-free case. How-

TABLE III. Particle parameters at injection, $T=1$. Dimensionless quantities (τ_p and d) are normalized by a reference time$=1$ s and a reference length$=0.390\,36$ m.

Case	Sh	τ_p	d	ρ_p/ρ	τ_p/τ_e	τ_p/τ_K	d/η	ϕ_v	ϕ_m	v_t/u_0^*	g_{x_i}
F	2	1.0	1.0×10^{-3}	1890	0.4140	2.330	0.1479	5.0×10^{-5}	0.1	0.0	
G	2	1.0	1.0×10^{-3}	1890	0.4140	2.330	0.1479	2.5×10^{-4}	0.5	0.0	
H	2	0.5	1.0×10^{-3}	945	0.2070	1.165	0.1479	1.0×10^{-4}	0.1	0.0	
I	2	0.25	1.0×10^{-3}	472.5	0.1035	0.583	0.1479	2.1×10^{-4}	0.1	0.0	
J	2	0.10	6.0×10^{-4}	525	0.0414	0.233	0.0887	1.9×10^{-4}	0.1	0.80	x_1
K	2	0.10	6.0×10^{-4}	525	0.0414	0.233	0.0887	1.9×10^{-4}	0.1	0.80	x_3

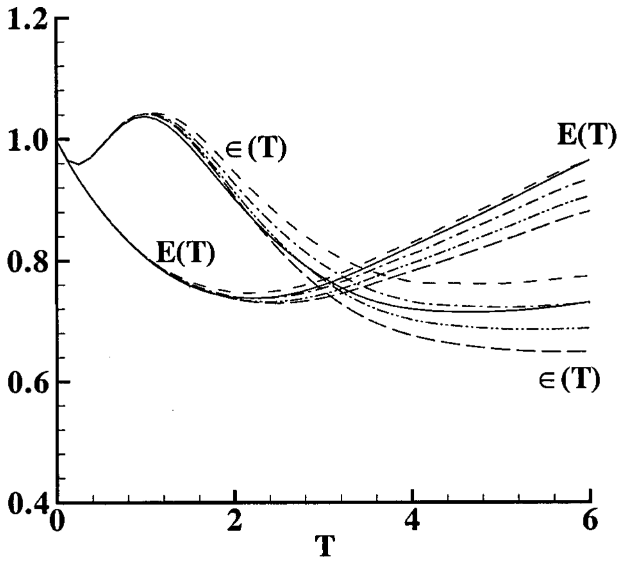

FIG. 45. Effect of particle inertia on the time development of $E(T)$ and its rate of dissipation $\epsilon(T)$. $\tau_p=0$ (solid lines), $\tau_p=0.1$ (dashed lines), $\tau_p=0.25$ (dash–dot lines), $\tau_p=1.0$ (long dashed lines).

ever, as the turbulence kinetic energy of the two-way coupling flow continues to decrease lower than (that of the particles-free case), $\epsilon(T)$ similarly decreases and becomes smaller than that of the particles-free case. The crossing-over time depends on the particle inertia. The particle with smallest inertia ($\tau_p=0.1$) did not show any reduction in $\epsilon(T)$ below that of the particles-free case (i.e., no crossing-over), since the turbulence kinetic energy is increased in the case as mentioned above.

Figure 46 shows the effect of varying the mass loading on the temporal development of the turbulence kinetic en-

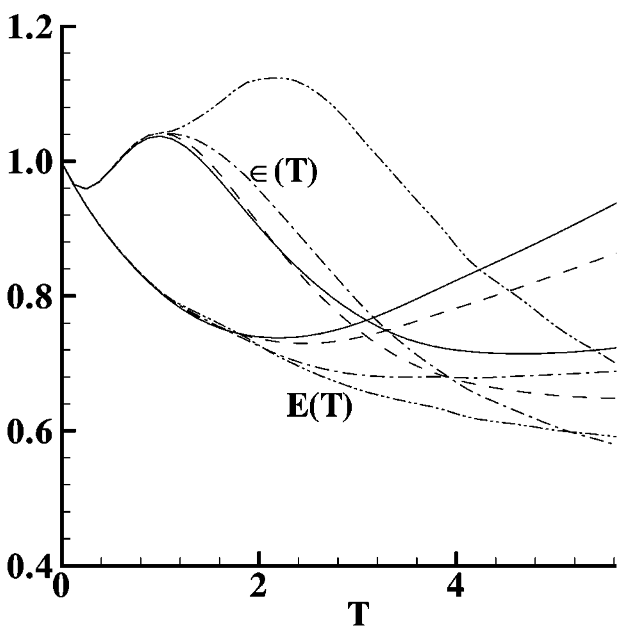

FIG. 46. Effect of particle's mass loading on the time development of $E(T)$ and its rate of dissipation $\epsilon(T)$, for the case with $\tau_p=1.0$. $\phi_m=0$ (solid lines), $\phi_m=0.1$ (dashed lines), $\phi_m=0.5$ (dash–dot lines), $\phi_m=1.0$ (dash–dot–dot lines).

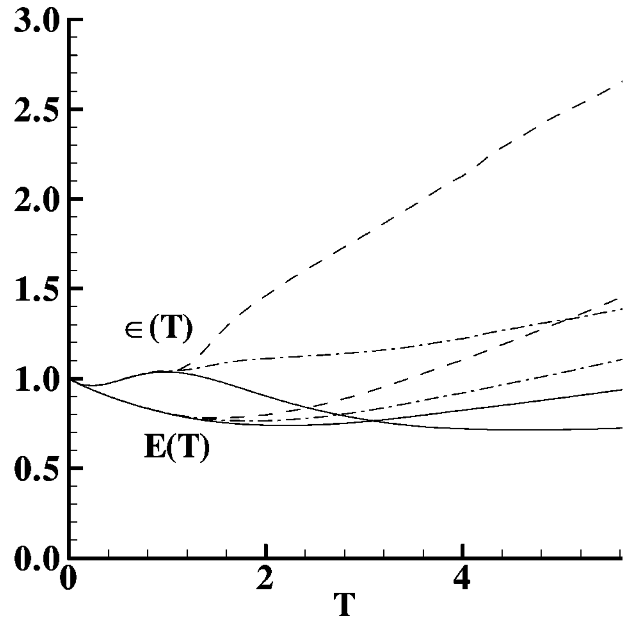

FIG. 47. Effect of particle's drift velocity on the time development of $E(T)$ and its rate of dissipation $\epsilon(T)$, for the case with gravity in the $-x_1$ direction. $v_t=0$ (solid lines), $v_t=0.25$ (dash–dot lines), $v_t=0.5$ (dashed lines).

ergy $E(T)$, and its rate of dissipation, $\epsilon(T)$. It is clear that, as the mass loading increases, the rate of turbulence modulation is increased. In all cases, the rate of turbulence dissipation, $\epsilon(T)$, is increased with the largest increase being for the case with mass loading of unity. However, as the turbulence kinetic energy is further reduced due to coupling, the turbulence dissipation is also reduced. The effect of varying particle drift velocity on the temporal development of the turbulence kinetic energy $E(T)$, and its rate of dissipation, $\epsilon(T)$ is shown in Figs. 47 and 48 for gravity in the $-x_1$ and $-x_3$ directions, respectively. It is seen that in both cases, the

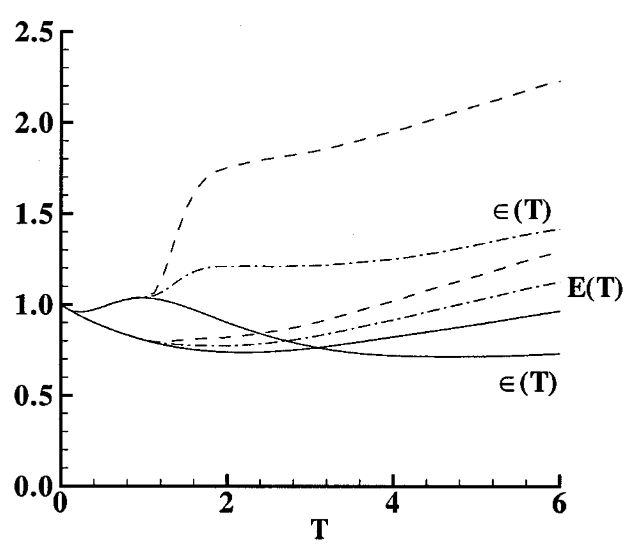

FIG. 48. Effect of particle's drift velocity on the time development of $E(T)$ and its rate of dissipation $\epsilon(T)$, for the case with gravity in the $-x_3$ direction. $v_t=0$ (solid lines), $v_t=0.25$ (dash–dot lines), $v_t=0.5$ (dashed lines).

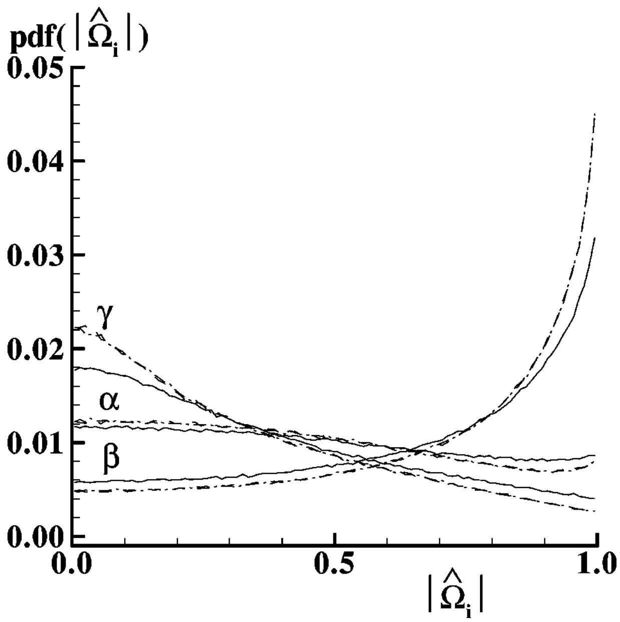

FIG. 49. Alignment of vorticity with the principal eigenvalues at $T=3$. Case B (solid lines), case C (dashed lines), case A (dash–dot lines).

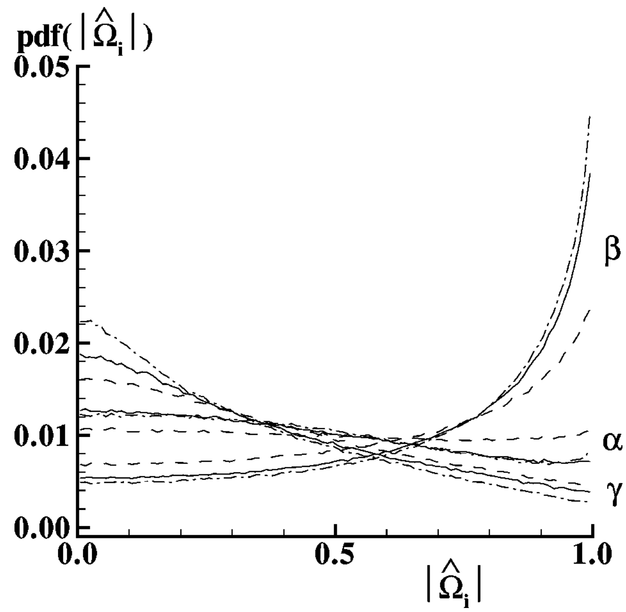

FIG. 50. Alignment of vorticity with the principal eigenvalues at $T=3$. Case D (solid lines), case E (dashed lines), case A (dash–dot lines).

increase in drift velocity increases both the turbulence kinetic energy and its rate of dissipation.

E. Modification of the alignment of vorticity and strain eigenvectors

It has been established by many researchers (e.g., Kerr,[21] Ashurst *et al.*,[22] and She *et al.*[21–23]), that the vorticity vector in incompressible turbulent flows tends to align with the intermediate eigenvector (β) of the strain rate tensor S_{ij}. In this section we examine the effects of dispersed particles on modifying this alignment.

Figure 49 shows the pdf of cosine the angle between the vorticity vector and the principal directions ($\mathbf{e}_\alpha, \mathbf{e}_\beta, \mathbf{e}_\gamma$) for cases A–C at $T=3$. It is seen that, for the uncoupled flow, the vorticity vector is aligned with the intermediate eigenvector, $\mathbf{e}_\beta$, as stated earlier. In case C, where τ_p and mass loading are small, the effect of coupling on the alignment is small at all times. In case B, where the particle inertia and mass loading are large, the alignment of the vorticity vector with the intermediate eigenvector, $\mathbf{e}_\beta$ is reduced, while the alignments with the other two eigenvalues are increased. Similar results are seen in Fig. 50 for cases D (gravity in the $-x_1$ direction) and E (gravity in the $-x_3$ direction) as compared to case A (particles-free flow). The decrease in alignment of the vorticity vector with $\mathbf{e}_\beta$ is largest for case E at all times.

In order to understand the reason for this change in alignment we derived the evolution equation of cosine the angle between the vorticity vector and the principal eigenvectors in strain coordinates (i.e., where the strain tensor is diagonal). This equation was first derived by Dresselhaus and Tabor[24] for flows *without particles*. The evolution equation for the absolute of cosine the angle between vorticity vector and principal strain eigenvectors ($|\hat{\Omega}_{(i)}|$) is re-derived here to include the particles effect. This equation is

$$\frac{D|\hat{\Omega}_{(i)}|}{Dt}=s_i|\hat{\Omega}_{(i)}|-\zeta^i_{\text{vorticity}}|\hat{\Omega}_{(i)}|-[\mathbf{\Omega}'\times\hat{\mathbf{\Omega}}]_{(i)}\frac{|\hat{\Omega}_{(i)}|}{\hat{\Omega}_{(i)}}-[(\hat{\mathbf{c}}\times\hat{\mathbf{\Omega}})\times\hat{\mathbf{\Omega}}]_{(i)}\frac{|\hat{\Omega}_{(i)}|}{\hat{\Omega}_{(i)}}, \tag{35}$$

where there is no summation on (i). s_i are the strain rate eigenvalues, such that $s_1=\alpha$ (the extensional strain), $s_2=\beta$ (the intermediate strain) and $s_3=\gamma$ (the compressive strain). The eigenvalues are ordered such that $\alpha\geqslant\beta\geqslant\gamma$ and $\alpha+\beta+\gamma=0$. The vorticity exponential-stretching rate $\zeta^i_{\text{vorticity}}$ is calculated from

$$\zeta^i_{\text{vorticity}}=s_i\hat{\Omega}_i^2. \tag{36}$$

$\mathbf{\Omega}'$ is the strain rotation vector. $\hat{\mathbf{c}}$ is a vector representing a source term due to direct particles effect on the alignment. The components of $\hat{\mathbf{c}}$ are calculated from

$$\hat{c}_i=\xi_{ij}b_j/|\boldsymbol{\omega}|, \tag{37}$$

where b_j is calculated from (27); ξ_{ij} is the j's component of the eigenvector i, and $|\boldsymbol{\omega}|$ is the magnitude of the vorticity vector. For a detailed derivation of (35) the reader is referred to Ahmed.[16]

The changes in the magnitudes of the terms on the RHS of (35) directly affect the alignment between the vorticity vector and the principal strain directions. The increase in vorticity stretching [second term of (35)] increases the vorticity alignment with the extensional strain direction, while the increase in the rotational term [third term in (35)] decreases this alignment. The last term on the RHS of (35) acts as an additional rotational term, i.e., the increase in this term reduces the alignment.

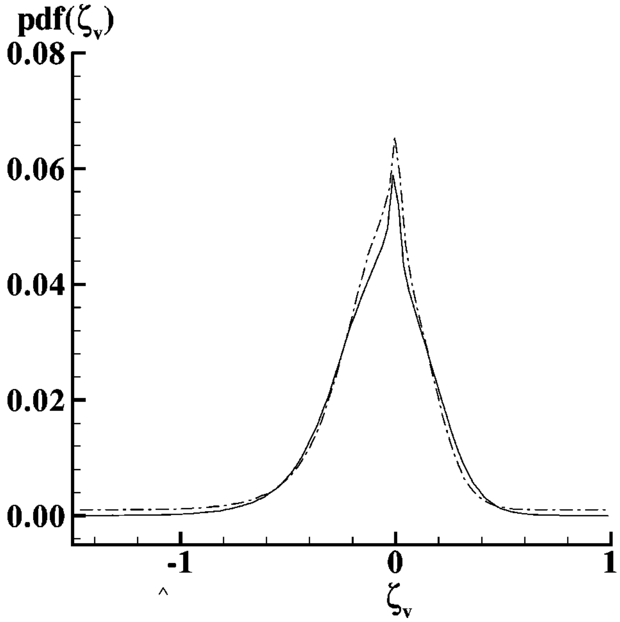

FIG. 51. pdf(ζ_v) in β-strain direction at $T=3$. Case B (solid line), case A (dash–dot line).

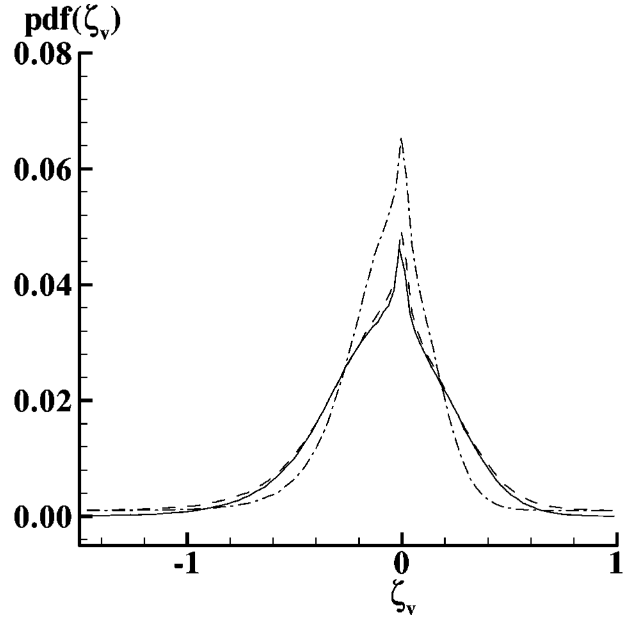

FIG. 52. pdf(ζ_v) in β-strain direction at $T=3$. Case D (solid line), case E (dashed line), case A (dash-dot line).

Now, we examine these terms with the objective of finding out why the particles reduce the alignment between vorticity vector and the intermediate eigenvector (β). It was shown earlier, that the magnitudes of the strain eigenvalues are increased due to coupling (Figs. 15 and 16), thus increasing the alignment of vorticity and strain eigenvectors (35). Similarly, the increase in the vorticity stretching $\zeta^i_{\text{vorticity}}$ in the equation of ($|\hat{\Omega}_{(2)}|$) increases the alignment of the vorticity vector and the intermediate eigenvector. Figure 51 shows the pdf($\zeta^i_{\text{vorticity}}$) for cases A (particles-free flow) and B (large particle inertia and mass loading) at $T=3$. The figure shows that the value of $\zeta^i_{\text{vorticity}}$ of case B is overlapping that of case A. However, the average value of $\zeta^i_{\text{vorticity}}$ of case B is larger than that of case A, signifying an increase in $\zeta^i_{\text{vorticity}}$ of case B as compared to that of case A on average. Similar results are shown in Fig. 52 for cases D (gravity in the $-x_1$ direction) and E (gravity in the $-x_3$ direction) at $T=3$. It is seen that case D has the largest increase in $\zeta^i_{\text{vorticity}}$, which is consistent with the reduced alignment in case D compared to case E shown earlier. However, the rotational term which reduces this alignment is increased due to coupling at $T=3$ as seen in Fig. 53 for case B and Fig. 54 for cases D and E. It should be noted that the rotational term is one order of magnitude larger than the other terms, and it exhibits the largest increase due to coupling. Moreover, the particles source term at $T=3$, seen in Fig. 55 for cases B, D, and E acts as an additional rotational term and thus reduces the alignment between vorticity and the intermediate eigenvector, $\mathbf{e}_\beta$. Thus, the main reason for the reduction in the alignment between vorticity and the intermediate eigenvector is due to the increase in rotational term and particles source term in Eq. (35). It should be noted that the vorticity rotational term [third term in (35)] is a function of vorticity and strain rate squared (see Dresselhaus and Tabor[24]). Since the dispersed particles increase the magnitude of these two fields, the vorticity rotation term increases. Also, the particle source term is function of vorticity which increased in our flow due to the coupling.

IV. CONCLUSIONS

Our DNS study has been conducted to understand the physical mechanisms responsible for modifying the turbulence structure by dispersed solid particles in a homogeneous turbulent shear flow. Our simulations show that particles increase the local velocity gradients, thus augmenting the local strain rate, which in turn increases the turbulence energy

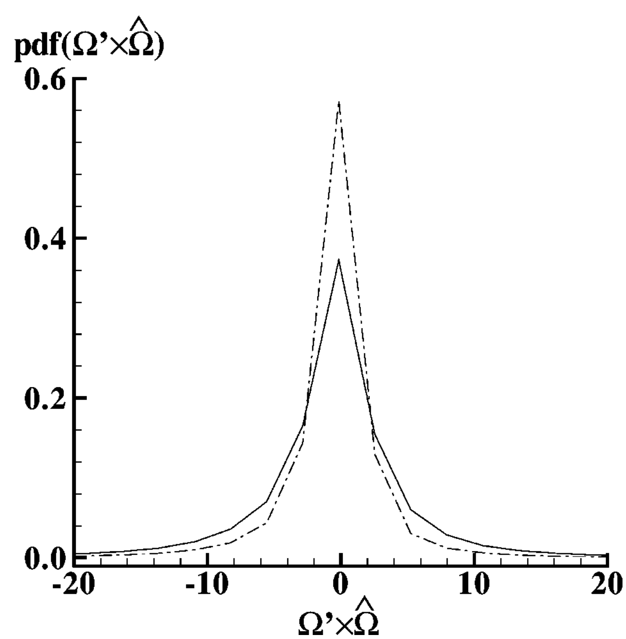

FIG. 53. pdf($\Omega' \times \hat{\Omega}$) in β-strain direction at $T=3$. Case B (solid line), case A (dash–dot line).

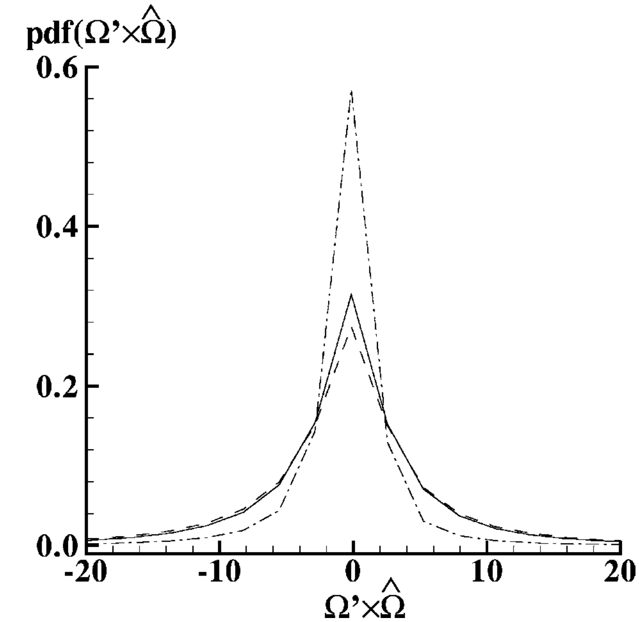

FIG. 54. pdf($\Omega' \times \hat{\Omega}$) in β-strain direction at $T=3$. Case D (solid line), case E (dashed line), case A (dash–dot line).

dissipation rate. The preferential accumulation of particles in low vorticity regions further increases the local velocity gradients, thus modifying the vorticity dynamics. It is known that regions of large production rate of turbulence energy are sandwiched between counter rotating vortices whose vorticity, ω_s, is aligned with the axis of the longitudinal vortex tubes. These longitudinal vortex tubes are strongly inclined toward the streamwise direction due to the imposed mean shear. The stronger ω_s is, the larger the production rate. The dispersed solid particles modify the alignment of the vorticity vector, $\boldsymbol{\omega}$, with the axis of the longitudinal vortex tube.

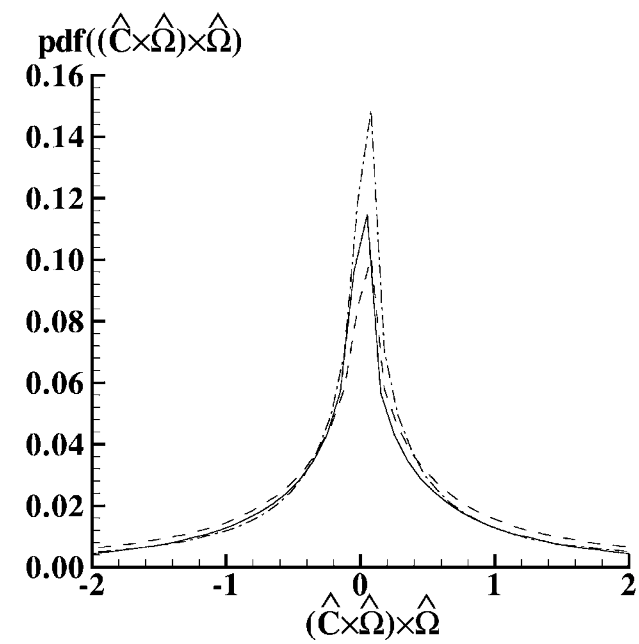

FIG. 55. pdf of the source term in β-strain direction at $T=3$. Case D (solid line), case E (dashed line), case B (dash–dot line).

Increasing the alignment between the vorticity vector and the axis of the longitudinal vortex tube increases ω_s, which in turn increases the turbulence production rate, and vice versa. Another effect is the reduction of the alignment between vorticity and the intermediate eigenvector (β) direction of the strain. This reduction is due to an increase in the rotational and particle source terms in the equation for the cosine of the angle between vorticity vector and the intermediate strain eigenvector.

ACKNOWLEDGMENT

This work was supported by NASA Grant No. NAG3-1831.

APPENDIX: PARTICLE'S SOURCE TERM IN THE COUPLED MOMENTUM EQUATION

In order to find an expression for the source term f_i in Eq. (2), we start from the instantaneous momentum equations of fluid and particle. The instantaneous fluid momentum equation is

$$\rho \frac{D\tilde{u}_i}{Dt} = \mu \frac{\partial^2 u_i}{\partial x_j^2} - \frac{\partial P}{\partial x_i} - \rho g \delta_{ik} + \tilde{f}_i, \tag{A1}$$

where $\tilde{f}_i$ is the instantaneous particle's source term which can be calculated from the instantaneous particle equation of motion

$$m_p(d\tilde{v}_i/dt_p) = m_p(\tilde{u}_i - \tilde{v}_i)/\tau_p - m_p g \delta_{ik}. \tag{A2}$$

The force exerted on the fluid by the particles is opposite to that of the drag force exerted on the particles by the fluid (Newton's third law). Thus $\tilde{f}_i$ is given by

$$\tilde{f}_i = -\rho_p \phi_v (d\tilde{v}_i/dt_p + g\delta_{ik}), \tag{A3}$$

where ϕ_v is local volume fraction of the particles. Now, we prescribe a reference state where $\tilde{u}=0$ and $\phi_v = \overline{\phi_v}$, where $\overline{\phi_v}$ is the particles volume fraction calculated from

$$\overline{\phi_v} = \frac{N_p(4/3)\,\pi a^3}{2}, \tag{A4}$$

where the factor of 2 in the denominator of Eq. (A4) is the dimensionless volume of our computational domain, and a is the particle radius. Also, at the reference state $\tilde{v}_i = v_t$, the particle's terminal velocity, and $d\tilde{v}_i/dt_p = 0$. Substituting in Eq. (A1), we get

$$0 = -\frac{\partial P_0}{\partial x_i} - \rho g \delta_{ik} - \rho_p \overline{\phi_v} g \delta_{ik}. \tag{A5}$$

Substituting for P in (A1) from $P = P_0 + p$, and the reference state (A5) is subtracted from (A1), we obtain in nondimensional form

$$\frac{D\tilde{u}_i}{Dt} = \frac{1}{\mathrm{Re}} \frac{\partial^2 u_i}{\partial x_j^2} - \frac{\partial p}{\partial x_i} - \frac{\rho_p}{\rho} \overline{\phi_v} g \delta_{ik} + \frac{\tilde{f}_i}{\rho}, \tag{A6}$$

Comparing Eq. (2) with (A6), where the left-hand-side (LHS) is the same in both, and using (A3) for $\tilde{f}_i$, we obtain the following expression for $-f_i$:

$$-f_i=\frac{\rho_p}{\rho}\overline{\phi_v}g\,\delta_{ik}-\frac{\rho_p}{\rho}\phi_v g\,\delta_{ik}-\frac{\rho_p}{\rho}\phi_v\frac{d\tilde{v}_i}{dt}. \tag{A7}$$

It should be noted that this expression can be used to obtain the particle's source term, S_p, in the coupled equation for the case of zero gravity [Eqs. (10) and (11)]. When $g=0$, the particle's source term becomes

$$-f_i=-\frac{\rho_p}{\rho}\phi_v\frac{d\tilde{v}_i}{dt}. \tag{A8}$$

Substituting for $d\tilde{v}_i/dt$ from Eq. (A2), taking into account that $g=0$, we get

$$-f_i=-\phi_m(u_i-v_i)/\tau_p, \tag{A9}$$

where $\phi_m=\rho_p\phi_v/\rho$. Multiplying Eq. (A9) by u_i and ensemble averaging, we obtain Eq. (11).

[1] M. M. Rogers and J. K. Eaton, ''The effect of small particles on fluid turbulence in a flat-plate turbulent boundary layer in air,'' Phys. Fluids A **3**, 928 (1991).
[2] M. Rashidi, G. Hetsroni, and S. Banerjee, ''Particle-turbulence interaction in a boundary layer,'' Int. J. Multiphase Flow **16**, 935 (1990).
[3] J. B. Mclaughlin, ''Numerical computation of particle-turbulence interaction,'' Int. J. Multiphase Flow **20s**, 211 (1994).
[4] K. D. Squires and J. K. Eaton, ''Particle response and turbulence modification in isotropic turbulence,'' Phys. Fluids A **2**, 1191 (1990).
[5] S. Elghobashi and G. C. Truesdell, ''Direct simulation of particle dispersion in a decaying isotropic turbulence,'' J. Fluid Mech. **212**, 655 (1992).
[6] M. R. Maxey, B. K. Patel, E. J. Chang, and L-P. Wang, ''Simulations of dispersed turbulent multiphase flow,'' Fluid Dyn. Res. **20**, 143 (1997).
[7] Y. Pan and S. Banerjee, ''Numerical simulation of particle interactions with wall turbulence,'' Phys. Fluids **8**, 2733 (1996).
[8] F. Mashayek, ''Droplet-turbulence interaction in low-Mach-number homogeneous shear two-phase flows,'' J. Fluid Mech. **367**, 163 (1998).
[9] R. J. Adrian and P. Moin, ''Stochastic estimation of organized turbulent structure: Homogeneous shear flow,'' J. Fluid Mech. **190**, 531 (1988).
[10] S. Kida and M. Tanaka, ''Reynolds stress and vortical structures in a uniformly sheared turbulence,'' J. Phys. Soc. Jpn. **61**, 4400 (1992).
[11] M. R. Maxey and J. J. Riley, ''Equation of motion for a small rigid sphere in a nonuniform flow,'' Phys. Fluids **26**, 883 (1983).
[12] T. Gerz, U. Schumann, and S. E. Elghobashi, ''Direct numerical simulation of stratified homogeneous turbulent shear flows,'' J. Fluid Mech. **200**, 563 (1989).
[13] G. C. Truesdell, ''The interaction between decaying isotropic turbulence and dispersed solid particles,'' Ph.D. thesis, University of California, Irvine, 1993.
[14] J. A. Domaradzki, R. S. Rogallo, and A. A. Wray, *Interscale energy transfer in numerically simulated turbulence* (Center for Turbulence Research, Stanford University, 1990), p. 319.
[15] R. G. Deissler, ''Effects of inhomogeneity and of shear flow in weak turbulent fields,'' Phys. Fluids **4**, 1187 (1961).
[16] A. M. Ahmed, ''The interaction between dispersed particles and homogeneous turbulent shear flows,'' Ph.D. dissertation, University of California, Irvine, 1998.
[17] L. Wang and M. R. Maxey, ''Settling velocity and concentration distribution of heavy particles in homogeneous isotropic turbulence,'' J. Fluid Mech. **256**, 27 (1993).
[18] S. Kida and M. Tanaka, ''Dynamics of vortical structures in a homogeneous shear flow,'' J. Fluid Mech. **274**, 43 (1994).
[19] H. Miura and S. Kida, ''Identification of tubular vortices in turbulence,'' J. Phys. Soc. Jpn. **66**, 1331 (1997).
[20] S. K. Lele, ''Vorticity form of turbulence transport equations,'' Phys. Fluids A **4**, 1767 (1992).
[21] R. M. Kerr, ''Histograms of helicity and strain in numerical turbulence,'' Phys. Rev. Lett. **59**, 783 (1987).
[22] W. T. Ashurst, A. R. Kerstein, and C. H. Gibson, ''Histograms of helicity and strain in numerical turbulence,'' Phys. Fluids **30**, 2343 (1987).
[23] W. T. She, S. E. Jackson, and S. A. Orszag, ''Structure and dynamics of homogeneous turbulence: Models and simulations,'' Proc. R. Soc. London, Ser. A **434**, 101 (1991).
[24] E. Dresselhaus and M. Tabor, ''The kinematics of stretching and alignment of material elements in general flow fields,'' J. Fluid Mech. **236**, 415 (1991).
[25] O. A. Druzhinin and S. Elghobashi, ''On the decay rate of isotropic turbulence laden with microparticles,'' Phys. Fluids **11**, 602 (1999).